Effects of ^{238}U variability and physical transport on water column ^{234}Th downward fluxes in the coastal upwelling system off Peru

Ruifang C. Xie[1]*, Frédéric A. C. Le Moigne[2], Insa Rapp[1], Jan Lüdke[1], Beat Gasser[3], Marcus Dengler[1], Volker Liebetrau[1], Eric P. Achterberg[1]

[1]GEOMAR Helmholtz Center for Ocean Research Kiel, Wischhofstrasse 1-3, 24148 Kiel, Germany

[2]Mediterranean Institute of Oceanography (UM 110, MIO), CNRS, IRD, Aix Marseille Université, Marseille, France

[3]IAEA Environment Laboratories, 4 Quai Antoine 1er, 98000 Monaco Monaco

* corresponding author: rxie@geomar.de

Abstract

The eastern boundary region of the southeastern Pacific Ocean hosts one of the world's most dynamic and productive upwelling systems with an associated oxygen minimum zone (OMZ). The variability in downward export fluxes in this region, with strongly varying surface productivity, upwelling intensities and water column oxygen content, is however poorly understood. Thorium-234 (^{234}Th) is a powerful tracer to study the dynamics of export fluxes of carbon and other elements, yet intense advection and diffusion in nearshore environments impact the assessment of depth-integrated ^{234}Th fluxes when not properly evaluated. Here we use VmADCP current velocities, satellite wind speed and *in situ* microstructure measurements to determine the magnitude of advective and diffusive fluxes over the entire ^{234}Th flux budget at 25 stations from 11°S to 16°S in the Peruvian OMZ. Contrary to findings along the GEOTRACES P16 eastern section, our results showed that weak surface wind speed during our cruises induced low upwelling rates and minimal upwelled ^{234}Th fluxes, whereas vertical diffusive ^{234}Th fluxes were important only at a few shallow shelf stations. Horizontal advective and diffusive ^{234}Th fluxes were negligible because of small alongshore ^{234}Th gradients. Our data indicated a poor correlation between seawater ^{238}U activity and salinity. Assuming a linear relationship between the two would lead to significant underestimations of the total ^{234}Th flux by up to 40% in our study. Proper evaluation of both physical transport and variability in ^{238}U activity is thus crucial in coastal ^{234}Th flux studies. Finally, we showed large temporal variations on ^{234}Th residence times across the Peruvian upwelling zone, and cautioned future carbon export studies to take these temporal variabilities into consideration while evaluating carbon export efficiency.

Keywords: eastern tropical South Pacific, ^{234}Th tracer, uranium-salinity correlation, physical processes, residence time

1. Introduction

Isotopes of thorium (Th) are widely used as tracers for particle cycling in the oceans (Waples et al., 2006). In particular, ^{234}Th has been extensively used to trace particle dynamics and export fluxes in the upper ocean, and to quantify the marine budgets of important macro- and micronutrients such as carbon (C), nitrogen (N), phosphorus (P) and iron (Fe) (e.g. Bhat et al., 1968; Buesseler et al., 1992; Coale and Bruland, 1987; Lee et al., 1998; Le Moigne et al., 2013; Cochran and Masqué, 2003; Van Der Loeff et al., 2006; Black et al., 2019). ^{234}Th has a relatively short half-life ($\tau_{1/2}$ = 24.1 days) that allows studies of biological and physical processes occurring on timescales of days to weeks. Unlike its radioactive parent uranium-238 (^{238}U, $\tau_{1/2}$ = 4.47 Ga) that is soluble in seawater, ^{234}Th is highly particle reactive with a particle-water partition coefficient of 10^3 to 10^8 (Santschi et al., 2006 and references therein) and is thus strongly scavenged by particles (Bhat et al., 1968). Generally, a deficit of ^{234}Th relative to ^{238}U is observed in the surface ocean and reflects net removal of ^{234}Th due to particle sinking, whereas secular equilibrium between ^{234}Th and ^{238}U is observed for intermediate and deep waters. Integrating this surface ^{234}Th deficit with depth yields the sinking flux of ^{234}Th and, if elemental:^{234}Th ratios are known, the sinking flux of elements such as C, N, P, Si and trace metals (e.g. Bhat et al., 1968; Buesseler et al., 1998; Buesseler et al., 1992; Coale and Bruland, 1987; Weinstein and Moran, 2005; Buesseler et al., 2006; Owens et al., 2015; Black et al., 2019; Puigcorbé et al., 2020).

Various ^{234}Th models have been put forward to study adsorption/desorption, aggregation and export, but single box models that assume negligible ^{234}Th fluxes due to physical transport are commonly used to calculate oceanic ^{234}Th-derived particle fluxes (see detailed review by Savoye et al., 2006). This assumption is typically appropriate in open ocean settings where ^{234}Th fluxes due to advection and diffusion are small relative to the downward fluxes of ^{234}Th associated with particle sinking. However, in upwelling regions

such as the equatorial Pacific and coastal systems, advective and diffusive ^{234}Th fluxes may become increasingly important (e.g., Bacon et al., 1996; Buesseler et al., 1998; Buesseler et al., 1995; Dunne and Murray, 1999). For example, in the equatorial Pacific, strong upwelling post El-Niño could account for ~50% of the total ^{234}Th fluxes (Bacon et al., 1996; Buesseler et al., 1995). Ignoring the upwelling term could thus lead to an underestimation of ^{234}Th fluxes by a factor of 2. Conversely, horizontal diffusion carrying recently upwelled, ^{234}Th-replete waters has been shown to balance the upwelled ^{234}Th fluxes in the central equatorial Pacific (Dunne and Murray, 1999). To the contrary, advective and diffusive ^{234}Th fluxes were minimal off the Crozet Islands in the Southern Ocean due to limited horizontal ^{234}Th gradients, long residence time of water masses, and low upwelling rates and diffusivities (Morris et al., 2007).

The dynamic nature of coastal processes requires that physical terms should be included in ^{234}Th flux calculation whenever possible. Accurate measurements of current velocities and diffusivities are however challenging and thus direct observations of the effects of physical processes on ^{234}Th distributions in coastal regions are scarce. Limited studies have incorporated advection and diffusion in the nearshore zones of the Arabian Sea (Buesseler et al., 1998), Gulf of Maine (Gustafsson et al., 1998; Benitez-Nelson et al., 2000), the South China Sea (Cai et al., 2008) and Peruvian oxygen minimum zone (OMZ) (Black et al., 2018). In the Arabian Sea, coastal upwelling during the southwest monsoon season could account for over 50% of the total ^{234}Th flux (Buesseler et al., 1998). Horizontal advection has been shown to be substantial in the Inner Cosco Bay of the Gulf of Maine (Gustafsson et al., 1998), whereas offshore advection and diffusion are only important in late summer (Benitez-Nelson et al., 2000). Therefore, the importance of physical processes on the ^{234}Th flux estimate is highly dependent on the seasonal and spatial variability of the current velocities, diffusivities and ^{234}Th gradients. In terms of the Peruvian OMZ, Black et al. (2018) showed that coastal

upwelling accounts for >50% of total ^{234}Th fluxes at 12°S; however, how upwelling ^{234}Th fluxes vary seasonally and spatially in this region is unclear.

Another uncertainty in ^{234}Th flux calculations in such region stems from variations on dissolved ^{238}U activities. Generally speaking, U behaves conservatively under open ocean oxic conditions and is linearly correlated with salinity (Chen et al., 1986; Ku et al., 1977; Owens et al., 2011). However, numerous studies have shown that such correlation breaks down in various marine environments including the tropical Atlantic (Owens et al., 2011), Mediterranean Sea (Schmidt and Reyss, 1991), and Arabian Sea (Rengarajan et al., 2003). Although it is generally accepted that deviations from the linear ^{238}U-S correlation will lead to differences in the final calculated ^{234}Th fluxes, there is currently little knowledge on how significant these differences could be.

In this study, we report vertical profiles of ^{234}Th and ^{238}U along four transects perpendicular to the coastline of Peru (i.e. shelf-offshore transects). We evaluate the ^{238}U-S correlation in low-oxygen waters and how deviations from this correlation impact final ^{234}Th flux estimates. We also assess the spatial and temporal importance of advection and diffusion on ^{234}Th flux estimates.

2. Sampling and methods

2.1 Seawater sampling and analysis

Seawater samples were collected at 25 stations along 4 shelf-offshore transects between 11°S and 16°S in the Peruvian OMZ during two cruises M136 and M138 on board the RV Meteor (Figure 1). Cruise M136 took place in austral autumn (April 11 to May 3, 2017) along two main transects at 12°S and 14°S (Dengler and Sommer, 2017). Two stations from M136 (stations 458 and 495) were reoccupied within a week (repeat stations 508 and

516, respectively) to evaluate the steady-state assumption in the ^{234}Th flux calculation. The surface sample of the repeat station 508 (reoccupied 4.5 days after station 458) was missing so only results from repeat stations 495 and 516 (occupation interval 1.5 days) were compared and discussed in terms of the non-steady state model (section 3.3). ^{234}Th sampling during cruise M138 was carried out in austral winter (June 1 to July 4, 2017) and focused on four shelf-offshore transects at 11°S, 12°S, 14°S and 16°S.

At each station, a stainless-steel rosette with Niskin bottles (Ocean Test Equipment®) was deployed for sampling of total ^{234}Th in unfiltered seawater and dissolved ^{238}U (0.2 μm pore size, Acropak® polycarbonate membrane). High vertical resolution sampling was performed in the upper 200 m where most of the biological activity occurs; additional depths were sampled down to 600 m, or 50 m above the seafloor. Deep seawater at 1000 m, 1500 m, and 2000 m was sampled at three stations to determine the absolute β counting efficiency. Salinity, temperature, oxygen concentrations and fluorescence data (Table S1) were derived from the sensors (Seabird Electronics® 9plus system) mounted on the CTD frame (Krahmann, 2018; Lüdke et al., in review 2020).

Sample collection and subsequent chemical processing and analysis for total ^{234}Th followed protocols by Pike et al. (2005) and SCOR Working Group RiO5 cookbook (https://cmer.whoi.edu/). Briefly, a ^{230}Th yield tracer (1 dpm) was added to each sample (4 L) before Th was extracted with MnO_2 precipitates. Precipitates were filtered onto 25 mm quartz microfiber filters (Whatman® QMA, 2.2 μm nominal pore size) and dried overnight at 50°C, after which they were counted at sea on a Risø® low-level beta GM multicounter until uncertainty was below 3%, and again 6 months later at home laboratory for background ^{234}Th activities. After the second beta counting, filters were digested in an 8M HNO_3/10% H_2O_2 solution (Carl Roth®, trace metal grade). 10 dpm of ^{229}Th was added to each sample at the beginning of digestion to achieve a 1:1 atom ratio between ^{229}Th:^{230}Th. Digested samples were diluted in a 2.5% HNO_3/0.01% HF mixture and ^{229}Th/^{230}Th ratios were measured using

an ICP-MS (ThermoFisher® Element XR) to determine the chemistry yield and final ^{234}Th activities. The average yield was calculated to be 97% ± 6% (n = 247). For a subset of samples (marked in Table S1) whose analysis failed during initial ICP-MS measurement, anion chromatography (Biorad® AG1x8, 100 – 200 mesh, Poly-Prep columns) was performed to remove Mn from the sample matrix before another ICP-MS analysis. This subset of samples also included three samples (marked in Table S1) whose initial ICP-MS measurement was successful, to test whether anion chromatography affects final ICP-MS results. Identical ^{229}Th/^{230}Th ratios were measured for samples with and without column chromatography (see Table S1 footnotes for details).

Each ^{238}U sample was acidified to pH ~1.6 at sea and transported home for analysis. Samples of dissolved ^{238}U were diluted 20 times in 1N HNO_3 at home laboratory and spiked with an appropriate amount of ^{236}U spike to achieve ^{236}U:^{238}U ~ 1:1. Ratios of ^{236}U:^{238}U were analyzed by ICP-MS (ThermoFisher Element XR) and activities of ^{238}U were calculated using isotope dilution. Seawater certified reference materials (CRMs), CASS-6 and NASS-7, and the International Association for the Physical Sciences of the Oceans (IAPSO) standard seawater were analyzed routinely for uranium concentrations.

2.2 Flux calculation

Assuming a one box model, the temporal change of ^{234}Th activities is balanced by production from ^{238}U, radioactive decay of ^{234}Th, removal of ^{234}Th onto sinking particles, and transport into or out of the box by advection and diffusion (Bhat et al., 1968; Savoye et al., 2006; and references therein):

$$\frac{\partial A_{Th}}{\partial t} = \lambda(A_U - A_{Th}) - P + V \quad (1)$$

where A_U and A_{Th} are respectively the activities of dissolved ^{238}U and total ^{234}Th, λ is the decay constant of ^{234}Th, P is the net removal flux of ^{234}Th, and V is the sum of advective and diffusive fluxes. It is recommended that the time interval between station occupations should be >2 weeks in order to adequately capture the temporal variability of the mean spatial gradients rather than small local changes (Resplandy et al., 2012). The solution of Eq. (1) (Savoye et al., 2006) is

$$P = \lambda \left[\frac{A_U\left(1-e^{-\lambda \Delta t}\right)+A_{Th1}\cdot e^{-\lambda \Delta t}-A_{Th2}}{1-e^{-\lambda \Delta t}} \right] \quad (2)$$

where Δt is the time interval between repeat occupations of a station; A_{Th1} and A_{Th2} are respectively total ^{234}Th activities during the first and second occupation. At times when repeat sampling is not possible within adequate cruise timeframe, steady state conditions are generally assumed, i.e. $\frac{\partial A_{Th}}{\partial t} = 0$. In this case, Eq. (1) is simplified into:

$$P = \int_0^z \lambda (A_U - A_{Th}) dz + V \quad (3)$$

The vertical flux of ^{234}Th, P (dpm m^{-2} d^{-1}), is integrated to the depth of interest. Earlier studies generally used arbitrarily fixed depths (e.g., the base of mixed layer or ML, and 100 m) for ^{234}Th and POC flux estimates (e.g., Bacon et al., 1996; Buesseler et al., 1992). Recent studies emphasized the need to normalize POC flux to the depth of euphotic zone (EZ), which separates the particle production layer in the surface from the flux attenuation layer below (Black et al., 2018; Buesseler and Boyd, 2009; Rosengard et al., 2015). In the open ocean, the depth of EZ is generally similar to ML depth. The PAR (Photosynthetically Active Radiation) sensor was not available during both of our cruises, so that it was not possible to identify the base of the EZ. For the purpose of this study, the slight difference of the exact depth chosen (ML vs. EZ) was of little relevance to the significance of physical processes and ^{238}U variability. Due to sampling logistics, however, we did not sample at the base of the ML, but 5-20 m below the ML. This depth corresponded closely to the EZ depth used in Black et al.

(2018) in the same study area during austral spring 2013. For the purpose of comparison with earlier studies which reported ^{234}Th fluxes at 100 m, we also calculated ^{234}Th fluxes at 100 m in this study.

2.3 Quantification of the physical fluxes

The physical term V in Eq. (2) is expressed as following:

$$V = \int_0^z \left(w\frac{\partial Th}{\partial z} - u\frac{\partial Th}{\partial x} - v\frac{\partial Th}{\partial y}\right)dz + \int_0^z \left(K_x\frac{\partial^2 Th}{\partial x^2} + K_y\frac{\partial^2 Th}{\partial y^2} - K_z\frac{\partial^2 Th}{\partial z^2}\right)dz \quad (3)$$

where *w* is the vertical (i.e. upwelling) velocity (m s^{-1}), u and v respectively the zonal and meridional current velocities (m s^{-1}), and K_x, K_y, and K_z represent eddy diffusivities (m^2 s^{-1}) in zonal, meridional and vertical directions, respectively. $\frac{\partial Th}{\partial z}$, $\frac{\partial Th}{\partial x}$ and $\frac{\partial Th}{\partial y}$ are vertical and horizontal ^{234}Th gradients (dpm L^{-1} m^{-1}), and $\frac{\partial^2 Th}{\partial x^2}$, $\frac{\partial^2 Th}{\partial y^2}$ and $\frac{\partial^2 Th}{\partial z^2}$ are respectively the second derivative of ^{234}Th (dpm L^{-1} m^{-2}) on the zonal, meridional and vertical directions.

2.3.1 Estimation of upwelling velocities

In the Mauritanian and Peruvian coastal upwelling regions, there is strong evidence that upwelling velocities in the mixed layer derived from satellite scatterometer winds and Ekman divergence (Gill, 1982) agree well with those from helium isotope disequilibrium (Steinfeldt et al., 2015). The parameterization by Gill (1982) considers the baroclinic response of winds blowing parallel to a coastline in a two-layer ocean. Vertical velocity (*w*) at the interface yields

$$w = \frac{\tau}{\rho f a} e^{-x/a} \quad (4)$$

where τ is the wind stress (kg m^{-1} s^{-2}) parallel to the coast line, ρ the water density (1023 kg m^{-3}), f the Coriolis parameter (s^{-1}) as a function of latitude, a the first baroclinic Rossby radius (km) and X the distance (km) to the coast.

Upwelling velocities were calculated at stations within 60 nautical miles (nm) of the coast, where upwelling is the most significant (Steinfeldt et al., 2015). We used a = 15 km for all stations based on the results reported by Steinfeldt et al. (2015) for the same study area. The magnitude of monthly wind stress was estimated from the monthly wind velocities (Smith, 1988):

$$\tau = \rho_{air} C_D U^2 \quad (5)$$

where ρ_{air} is the air density above the sea surface (1.225 kg m^{-3}), C_D the drag coefficient (10^{-3} for wind speed < 6 m s^{-1}), and U the wind speed.

Monthly wind speed (m s^{-1}) fields from MetOp-A/ASCAT scatterometer sensor with a spatial resolution of 0.25° (Bentamy and Croize-Fillon, 2010) were retrieved from the Centre de Recherche et d'Exploitation Satellitaire (CERSAT), at IFREMER, Plouzané (France) (data version numbers L3-MWF-GLO-20170903175636-01.0 and L3-MWF-GLO-20170903194638-01.0). We assumed a linear decrease of w from base of the mixed layer toward both the ocean surface and 240 m depth (bottom depth of our shallowest station). Upwelling rates at any depth between 0 and 240 m at individual stations could thus be determined once w was estimated. Following (Rapp et al., 2019), an error of 50% was assigned to estimated upwelling velocities to account for uncertainties associated with the spatial structure and temporal variability of the wind field, and the satellite wind product near the coast.

2.3.2 Estimation of upper-ocean velocities

231 During both cruises a phased-array vessel-mounted acoustic Doppler current profiler
232 (VmADCP; 75 kHz Ocean Surveyor, Teledyne RD-Instruments) continuously measured zonal
233 and meridional velocities in the upper 700 m of the water column (Lüdke et al., in review
234 2020). Post-processing of the velocity data included water track calibration and bottom
235 editing. After calibration, remaining uncertainty of hourly averages of horizontal velocities are
236 smaller than 3 cm s^{-1} (e.g. Fischer et al., 2003). For the horizontal advective flux calculation
237 (Eq. 3), velocities collected within a 10 km radian at inshore stations (St. 353, 428, 458, 475,
238 508, 904, and 907) and within a 50 km radian at offshore stations (Lüdke et al., in review
239 2020) were averaged. Data collected at the same positions within 5 days due to station repeats
240 were also included in the velocity average. As representative for the near-surface flow, we
241 extracted the velocity data from the top 30 m for M136 stations and top 50 m for M138 station
242 (defined as the "top layer" thereafter); these depths correspond to 5-20 m below the base of
243 the ML during each cruise.

244

245 2.3.3 Estimation of vertical and horizontal eddy diffusivities

246 While the strength of ocean turbulence determines the magnitude of diapycnal or
247 vertical eddy diffusivities, the intensity of meso- and submesoscale eddies determine the
248 magnitude of lateral eddy diffusivities. During the R/V Meteor cruise M136 and the follow up
249 cruise (M137) in the same region, the strength of upper-ocean turbulence was measured using
250 shear probes mounted to a microstructure profiler. The loosely-tethered profiler was
251 optimized to sink at a rate of 0.55 m s^{-1} and equipped with three shear sensors, a fast-response
252 temperature sensor, an acceleration sensor, two tilt sensors and conductivity, temperature,
253 depth sensors sampling with a lower response time. On transit between each CTD station 3 to
254 9 microstructure profiles were collected. Standard processing procedures were used to
255 determine the dissipation rate of turbulent kinetic energy (ε) in the water column (see

Schafstall et al., 2010 for detailed description). Subsequently, turbulent vertical diffusivities K_Z were determined from $K_z = \Gamma \varepsilon N^{-2}$ (Osborn, 1980), where N is stratification and Γ is the mixing efficiency for which a value of 0.2 was used following Gregg et al. (2018). Stratification (Buoyancy frequency) was calculated using CTD data retrieved from microstructure profilers and following the gsw_Nsquared function from the Gibbs Sea Water library (McDougall et al., 2009; Roquet et al., 2015). A running mean of 10 dbar was applied to avoid including unstable events due to turbulent overturns. The 95% confidence intervals for averaged K_z values were determined from Gaussian error propagation following Schafstall et al. (2010).

Altogether, 189 microstructure profiles were collected during M136 (Thomsen and Lüdke, 2018) and 258 profiles during the follow-up cruise M137 (unpublished data; May 6 – 29, 2017). An average turbulent vertical diffusivity profile was calculated each from all inshore (<500m water depth) and all offshore (>500m water depth) profiles (Figure S1). Microstructure profiles collected during cruise M138 were not available but there were little variations amongst the cruise average inshore and offshore microstructure profiles from M136 and M137 despite drastic change in the intensities of the poleward Peru Chile Undercurrent (Lüdke et al., in review 2020). It thus appears appropriate to apply these average vertical diffusivities also to stations during M138.

Horizontal eddy diffusivity could not be determined from data collected during the cruises. Surface eddy diffusivities in the North Atlantic OMZ were estimated to be on the order of a few 1000 $m^2 s^{-1}$ that decrease exponentially with depth (Hahn et al., 2014). Similar magnitude of eddy diffusivities was estimated for the ETSP based on surface drifter data and satellite altimetry (Abernathey and Marshall, 2013; Zhurbas and Oh, 2004). We thus consider an eddy diffusivity of 1000 $m^2 s^{-1}$ as a good approximate in this study for the evaluation of horizontal diffusive ^{234}Th fluxes.

281

282 2.4 Residence time of ^{234}Th

283 The residence time (τ_{Th}) of total ^{234}Th represents a combination of the time required
284 for the partition of dissolved ^{234}Th onto particulate matter and that for particle removal. In a
285 one-box model, the residence time of an element of interest can be estimated by determining
286 the standing stock of this element and the rates of elemental input to the ocean or the rate of
287 elemental removal from seawater to sediments (Bewers and Yeats, 1977; Zimmerman, 1976):

288 $$\tau_{Th} = \frac{A_{Th(mean)} \cdot Z}{P} \quad (6)$$

289 For the case of ^{234}Th, $A_{Th(mean)}$ is the averaged ^{234}Th activities of the surface layer, Z is
290 the depth of top layer, and P the removal flux of ^{234}Th.

291

292 **3. Results**

293 3.1 Profiles of dissolved ^{238}U, total ^{234}Th, oxygen and fluorescence

294 The vertical profiles of ^{238}U and ^{234}Th activities are shown in Figure 2 and tabulated in
295 Table S1. Data from station 508 were reported in Figure 2 and Table S1 but excluded in the
296 Discussion section, because the surface sample at 5 m from this station was missing, which
297 prevents any flux calculation. Also tabulated in Table S1 are temperature, salinity and
298 concentrations of oxygen and fluorescence obtained from the CTD sensors. Uranium
299 concentrations of CRMs and the IAPSO standard seawater are reported in Table S2.

300 Activities of ^{238}U showed small to negligible variations with depth, averaging 2.54 ±
301 0.05 dpm L^{-1} (or 3.28 ± 0.07 ng/g, 1SD, n = 247) at all stations. The vertical distributions of
302 ^{238}U did not appear to be affected by water column oxygen concentrations or the extent of
303 surface fluorescence maxima (Figure 2). Average U concentrations of both CASS-6 (2.77 ±

304 0.04 ng g^{-1}, 1SD, n = 5) and NASS-7 (2.86 ± 0.05 ng/g, 1SD, n = 5) measured in this study
305 agreed well with certified values (2.86 ± 0.42 ng g^{-1} and 2.81 ± 0.16 ng g^{-1}, respectively).
306 Average ^{238}U concentration measured in our IAPSO standard seawater (OSIL batch P156)
307 (3.24 ± 0.06 ng g^{-1}, 1SD, n = 27) is slightly higher than that reported in Owens et al. (2011)
308 (3.11 ± 0.03 ng g^{-1}, 1SD, n = 10, OSIL P149), and may reflect slight differences in U
309 concentrations between different OSIL batches.

310 Total ^{234}Th activities varied from 0.63 to 2.89 dpm L^{-1} (Figure 2). All stations showed
311 large ^{234}Th deficits in surface waters with $^{234}Th/^{238}U$ ratios as low as 0.25 (Figure 3). The
312 extent of surface ^{234}Th deficits did not vary as a function of depths of either mixed layer or the
313 upper oxic-anoxic interface, nor the magnitude of surface fluorescence concentrations (Table
314 1, Figure 2). ^{234}Th at all stations generally reached equilibrium with ^{238}U at depths between 30
315 m and 250 m (Table 1). The equilibrium depths were slightly shallower toward the shelf at the
316 11°S, 12°S and 16°S transects. At St. 912, deficits of ^{234}Th extended beyond 600 m depth
317 (Figure 2). The following stations (St. 428, 879, 898, 906, 907, 915, 919) displayed a
318 secondary ^{234}Th deficit below the equilibrium depth, indicative of ^{234}Th removal processes. A
319 small ^{234}Th excess at depth was only observed for St. 559 at 100 m. Ratios of $^{234}Th/^{238}U$ for
320 deep samples at 1000 m, 1500 m, and 2000 m varied between 0.95 and 1.02 (1.00 ± 0.04,
321 1SD, n = 11), suggesting that ^{234}Th was at equilibrium with ^{238}U at these depths.

322

323 3.2 Vertical and horizontal ^{234}Th gradients

324 Discrete vertical ^{234}Th gradients in each profile (or the curvature of the profile) were
325 estimated by the difference in ^{234}Th activities and that in sampling depths. As such, vertical
326 ^{234}Th gradients varied greatly amongst stations, and were larger at shallow depths ranging

from 0.003 dpm L^{-1} m^{-1} to 0.085 dpm L^{-1} m^{-1} (median 0.013 dpm L^{-1} m^{-1}). Vertical ^{234}Th gradients were essentially negligible at and below equilibrium depths.

While calculation of the vertical ^{234}Th gradient is straightforward, the same is hardly true for the determination of horizontal ^{234}Th gradient. Mean ^{234}Th activities in the top layer (see section 2.3.2 for depth definition) of the water column are highly variable amongst stations (Table 3, Figure 4), and likely reflect variations occurring at small temporal and spatial scales in the Peruvian OMZ. Quantification of the horizontal ^{234}Th gradient between individual station thus may not be adequate to evaluate large scale advection and eddy diffusion across the study area. Therefore, alongshore ^{234}Th gradients on a larger spatial scale (1° apart) were instead calculated by grouping stations into 1° by 1° grids and averaging ^{234}Th activities of each grid for the top layer. Alongshore ^{234}Th gradients in the top layer at nearshore stations for M138 are fairly consistent, ranging from 1.5×10^{-6} dpm L^{-1} m^{-1} to 1.7×10^{-6} dpm L^{-1} m^{-1}, with a slightly stronger gradient in the north compared to the south. The net difference in alongshore ^{234}Th gradient is merely 2×10^{-7} dpm L^{-1} m^{-1}. A slightly smaller alongshore ^{234}Th gradient of 4.8×10^{-7} dpm L^{-1} m^{-1} was observed for M136. The magnitude of the net difference in alongshore ^{234}Th gradient for M136 cannot be adequately quantified, due to smaller spatial sampling coverage. Judging on the similarity in the spatial distributions of mean ^{234}Th between cruises M136 and M138 (Figure 4), it is reasonable to assume that net difference in alongshore ^{234}Th gradient remained similar during both cruises.

3.3 Steady state vs. non-steady state models

The relative importance of ^{234}Th fluxes due to advection and diffusion were assessed here assuming steady state conditions, which assume negligible temporal ^{234}Th variability. But how valid is this assumption in the Peruvian upwelling zone? Profiles of temperature and oxygen at repeat stations 458 and 508 showed that a lightly cooler and oxygen-depleted water

mass dominated at the upper 50 m at station 508 (Figure 5). However, an assessment of the ^{234}Th fluxes at these two stations were not possible as the surface sample from station 508 was missing. Repeat stations 495 and 516 show substantial temporal variations in ^{234}Th activities at each sampled depth in the top 200 m, while temperature and salinity profiles confirmed that similar water masses were sampled during both occupations (Figure 5). Particularly, the surface ^{234}Th deficit was more intense at St. 495 (^{234}Th/^{238}U = 0.44) compared to St. 516 (^{234}Th/^{238}U = 0.73). Correspondingly, ^{234}Th fluxes decreased substantially from St. 495 to St. 516. At 100 m, the difference in ^{234}Th fluxes between these two stations was ~ 30% (3200 ± 90 dpm m^{-2} d^{-1} at St. 495 and 2230 ± 110 dpm m^{-2} d^{-1} at St. 516). At 200 m where ^{234}Th resumed equilibrium with ^{238}U at both stations, ^{234}Th flux difference was ~ 25% (4510 ± 220 dpm m^{-2} d^{-1} at St. 495 and 3455 ± 200 dpm m^{-2} d^{-1} at St. 516). Taking the non-steady state term in Eq. (1) into consideration (see details in Resplandy et al. (2012) and Savoye et al. (2006) for the derivation of flux formulation and error propagation) increased total ^{234}Th at St. 516 by 40% to 3110 ± 1870 dpm m^{-2} d^{-1} at 100 m (or 45% to 5040 ± 2290 dpm m^{-2} d^{-1} at 200 m), which is indistinguishable within error from fluxes at St. 495. The large errors associated with the non-steady state calculation due to the short duration between station occupations prevent a meaningful application of this model in the current study (also see discussion in Resplandy et al, 2012). As estimation of the physical fluxes is independent of the models chosen between steady and non-steady states, the following results and discussion sections regarding physical effects on the ^{234}Th flux estimates is based on the steady state model only.

3.4 Export fluxes of ^{234}Th

Fluxes of ^{234}Th due to radioactive production and decay (hereafter 'production flux'), upwelling, and vertical diffusion were reported in Table 1 and Figure 6 for both depths 5-20 m below the ML and at 100 m. The production fluxes of ^{234}Th at 5-20 m below the ML

ranged from 560 dpm m^{-2} d^{-1} to 1880 dpm m^{-2} d^{-1}, whereas at 100 m they were much higher at 850 dpm m^{-2} d^{-1} to 3370 dpm m^{-2} d^{-1}. There is no discernable trend regarding the production fluxes between the shelf and offshore stations, similar to those seen along the eastern GP16 transect (Black et al. 2017).

Alongshore winds were unusually weak off Peru preceding and during our sampling campaign as a result of the 2017 coastal El Niño (Echevin et al., 2018; Lüdke et al., in review 2020; Peng et al., 2019), which resulted in nominal upwelling in the water column. At nearshore stations, upwelling rates at the base of the ML varied between 1.3×10^{-7} m s^{-1} and 9.7×10^{-6} m s^{-1}, whereas upwelling rates at offshore stations were on the order of 10^{-10} m s^{-1} to 10^{-8} m s^{-1} and essentially negligible. As a result, upwelled ^{234}Th fluxes at 5-20 m below the ML were only significant at stations closest to shore; these stations were 428 (130 dpm m^{-2} d^{-1}), 883-12 (80 dpm m^{-2} d^{-1}) and 904-16 (280 dpm m^{-2} d^{-1}) whose upwelled ^{234}Th fluxes accounted for 10%, 11% and 25% of the total ^{234}Th fluxes respectively (Figure 6). Upwelled ^{234}Th fluxes at the rest of the stations accounted for less than 2% of the total ^{234}Th fluxes (6% at stations 353 and 907-11) and were insignificant. At 100 m, both vertical ^{234}Th gradients and upwelling rates were significantly smaller compared to shallower depths. As a result, upwelled ^{234}Th fluxes were less than 70 dpm m^{-2} d^{-1}, or less than 4% of total ^{234}Th fluxes.

Similarly, vertical diffusivities, shown as running mean over 20 m in Figure S1, were an order of magnitude higher at shallow stations ($3.2 \times 10^{-4} \pm 1.7 \times 10^{-4}$ m^2 s^{-1}; 1SD, 27 m to 100 m below sea surface) compared to those at deep stations ($1.7 \times 10^{-5} \pm 0.6 \times 10^{-5}$ m^2 s^{-1}; 1SD; 34 – 100 m below sea surface). Within the upper 27 m to 33 m layer at offshore deep stations, vertical diffusivities decreased exponentially by an order of magnitude within a few meters; below this depth, vertical diffusivities remained relatively stable (Figure S1). This is not surprising as wind-driven turbulent is most significant at the ocean surface (Buckingham et al., 2019). In this study, the sampling depths immediately below the ML were generally 30

m and 60 m. A few high vertical diffusivity values around 30 m at deep stations were unlikely representative for the 30 m – 60 m water column layer. We thus opted to only apply vertical diffusivities below 33 m at deep stations. Relative standard errors (RSE) associated with diffusivity estimates varied from 35% to 55%. Vertical diffusive ^{234}Th fluxes at 5-20 m below the ML, determined using both vertical diffusivity and vertical ^{234}Th gradient, varied greatly amongst stations. At shallow stations 428, 458, and 883-12, vertical diffusive ^{234}Th fluxes made up 37% (490 dpm m^{-2} d^{-1}), 14% (160 dpm m^{-2} d^{-1}), and 21% (160 dpm m^{-2} d^{-1}) of total ^{234}Th fluxes, respectively (Figure 6). At the rest of the stations, vertical diffusive ^{234}Th fluxes appeared to be insignificant, ranging between 1% and 10% in the total ^{234}Th flux budget. At 100 m, vertical diffusive ^{234}Th fluxes at station 428, 458, and 883-12 remained high at 390 dpm m^{-2} d^{-1}, 150 dpm m^{-2} d^{-1}, 120 dpm m^{-2} d^{-1}, respectively, whereas those at the rest of the stations accounted for < 2% of the total ^{234}Th flux.

Horizontal advective and diffusive ^{234}Th fluxes were both very small. Average alongshore current velocities (Lüdke et al., in review 2020) for the top layer varied from 0.06 m s^{-1} to 0.34 m s^{-1}. At the peripheral of a freshly-formed anticyclonic eddy (St. 915-1), alongshore current velocities could be as high as 0.53 m s^{-1}. Taking the mean alongshore velocity of 0.2 m s^{-1} and the net difference in alongshore ^{234}Th gradient of 2 x 10^{-7} dpm L^{-1} m^{-1}, the resulting net horizontal advective ^{234}Th flux at the top layer is ~ 50 dpm m^{-2} d^{-1}, a mere 3-9% of the total ^{234}Th fluxes.

Horizontal diffusive ^{234}Th flux was estimated using an average eddy diffusivity of 1000 m^2 s^{-1} (see Methods section 2.3.3) and the alongshore ^{234}Th gradient. A maximum value of 10 dpm m^{-2} d^{-1} was calculated, which accounted for <1% of total ^{234}Th flux at all stations. Note that the horizontal advective and lateral diffusive fluxes presented here are a rough estimate and should only provide an idea of their order of magnitude. Due to the uncertainty inherent to the estimates, we refrain from adding these values to Table 1.

4. Discussion

4.1 Lack of linear ^{238}U – salinity correlation in the Peruvian OMZ

The water column profiles of ^{238}U in the Peruvian OMZ (Figure 2) are similar to those seen in the open ocean (see compilations in Owens et al., 2011 and Van Der Loeff et al. (2006), and references therein). It thus appears that water column suboxic/anoxic conditions alone is not sufficient to remove U, in contrast to sedimentary U studies underlying low oxygen waters where soluble U(VI) diffused downward into subsurface sediments and reduced to insoluble U(IV) (Anderson et al., 1989; Böning et al., 2004; Scholz et al., 2011). Our inference is in accord with water column ^{238}U studies in intense OMZs in the eastern tropical North Pacific (Nameroff et al., 2002) and the Arabian Sea (Rengarajan et al., 2003), where ^{238}U concentrations remain constant over the entire upper water column studied.

Dissolved ^{238}U and salinity across the entire Peruvian OMZ displayed poor linear correlation regardless of seawater oxygen concentrations (Figure 7a-b). The general consensus is that U behaves conservatively in oxic seawater in the open ocean and early observations have shown that ^{238}U activities can be calculated from salinity based on a simple linear correlation between the two (e.g. Chen et al., 1986; Ku et al., 1977). Compilations in Van Der Loeff et al. (2006) and Owens et al. (2011) further demonstrated that the majority of uranium data points in the global seawater dataset follow a linear correlation with seawater salinity. The ^{238}U-salinity formulations from either Chen et al. (1986) or Owens et al. (2011) are thus generally appropriate for open ocean conditions and have been widely used in ^{234}Th flux studies. However, this linear ^{238}U-salinity correlation breaks down in the Peruvian OMZ. Furthermore, the measured ^{238}U activities in this study correlated poorly with those calculated from salinity using the Owens formulation regardless of water column oxygen concentrations (Table S2, Figure 7c), with the former significantly higher than the projected values and

differences up to 10%. Both evidences suggested that non-conservative processes have introduced significant amount of dissolved U into the water column.

It is likely that this poor ^{238}U-salinity correlation in the water column is not a unique feature off the coast of Peru. Poor correlations between dissolved ^{238}U and salinity have been previously observed in open ocean settings such as the Arabian Sea (Rengarajan et al., 2003) and the Pacific Ocean (Ku et al., 1977), and shelf-estuary systems such as the Amazon shelf (McKee et al., 1987; Swarzenski et al., 2004). It is possible that the narrow range of salinity within any single ocean basin precludes a meaningful ^{238}U-salinity correlation (Ku et al., 1977; Owens et al., 2011). For the Peruvian shelf system, two possible scenarios may further explain the lack of linear ^{238}U-salinity correlation in the water column. Firstly, authigenic U within the sediments may be remobilized under ENSO-related oxygenation events. In reducing pore water, U reduction and removal from pore water is usually seen within the Fe reduction zone (Barnes and Cochran, 1990; Barnes and Cochran, 1991; Scholz et al., 2011). As such, a downward diffusive flux of U across the water-sediment interface is expected in reducing sedimentary environment. However, pore water and bottom water geochemistry measurements during two previous cruises (M77-1 and M77-2) along an 11°S transect off Peru showed large diffusive fluxes of U out of the Peruvian shelf sediments despite that both Fe reduction and U reduction took place in the top centimeters of sediments (Scholz et al., 2011). It was suggested that a minute increase in bottom water oxygen concentration induced by El Niño events would be sufficient in shifting the U(VI)/U(IV) boundary by a few centimeters and remobilize authigenic U (Scholz et al., 2011). Preceding and during our sampling campaign, a coastal El Niño event, with coastal precipitation as strong as the 1997-98 El Niño event, had developed rapidly and unexpectedly in January, and disappeared by May 2017 during cruise M136 (Echevin et al., 2018; Garreaud, 2018; Peng et al., 2019). This strong coastal El Niño event could induce an oxygenation event large enough to remobilized

authigenic U along the Peruvian shelf. Secondly, resuspension of bottom sediments and subsequent desorption of U from ferric-oxyhydroxides could affect the ^{238}U-salinity relationship, similar to that seen on the Amazon shelf at salinity above 10 (McKee et al., 1987) and in laboratory experiments (Barnes and Cochran, 1993). Fe reduction and release from the Peruvian shelf sediments (Noffke et al., 2012; Scholz et al., 2014) could release additional U to overlying waters. The magnitude of such, however, has not been quantified.

The consequence of the notable difference between measured ^{238}U in this study and salinity-based ^{238}U to ^{234}Th flux according to Eq. (2) is neither linear nor straightforward, because the vertical gradients of both ^{238}U and ^{234}Th strongly affects the impacts of ^{238}U variations on ^{234}Th fluxes. In this study, ^{234}Th fluxes at 100 m derived from salinity-based ^{238}U lead to significant underestimation of ^{234}Th fluxes by an average of 20% and as high as 40% (Table 2). These differences in ^{234}Th fluxes will have direct consequences for ^{234}Th derived elemental fluxes such as C, N, P and trace metals. It is thus important to note that U concentrations in coastal systems are highly sensitive to bottom water oxygen concentrations and redox-related U addition, variability of which is expected to intensify with future climate change (Shepherd et al., 2017). Relatively minor variations in dissolved ^{238}U could account for substantial overestimation/underestimation of the depth-integrated ^{234}Th fluxes. We thus encourage future ^{234}Th flux studies in such environments to include seawater ^{238}U analysis.

4.2 Dynamic advective and diffusive ^{234}Th fluxes

The significance of advection and diffusion in the total ^{234}Th flux budget highly depends on the upwelling rate, current velocity, vertical diffusivity, and ^{234}Th gradient on the horizontal and vertical directions. Our results demonstrated that physical processes off Peru during and post the 2017 coastal El Niño have very limited impact on the downward fluxes of ^{234}Th (Figure 6).

Our findings are in reasonable agreement with those from the GEOTRACES GP16 eastern section along 12°S from Peru to Tahiti, in which Black et al. (2018) quantified both horizontal and vertical advective ^{234}Th fluxes. Horizontal advective fluxes for the upper 30 m water column estimated during GP16 were ~180 dpm m^{-2} d^{-1} for all nearshore and offshore stations, similar in magnitude to those estimated in our study (~50 dpm m^{-2} d^{-1}). Upwelling fluxes along GP16 eastern section was suggested to account for 50% to 80% of total ^{234}Th fluxes at the base of the euphotic zone (Black et al., 2018), a depth similar to or slightly deeper than ML depths in the current study where upwelling fluxes accounted for less than 25% of total ^{234}Th fluxes). Total ^{234}Th fluxes along the GP16 eastern section, ranging from 4000 to 5000 dpm m^{-2} d^{-1} at the base of the euphotic zone, were much higher than those in our study (560 to 1900 dpm m^{-2} d^{-1} 5-20 m below the ML). This difference could be related to the period of sampling (austral autumn and winter 2017 in our study *vs.* austral spring 2013 for the GP16 section). We note that the estimated vertical mixing rates based on ^{7}Be isotope at the base of the euphotic zone along the GP16 section (Kadko, 2017) were at least an order of magnitude higher than the upwelling rates at the base of the ML at nearby stations in our study. This difference could stem from different methods used to estimate upwelling rates at different timescales, and may also reflect the dynamic upwelling system off Peru in which upwelling rates vary greatly seasonally and interannually. During cruises M136 and M138, upwelling favorable easterly winds off Peru were weak, resulting in negligible coastal upwelling. Coastal upwelling in the same general area was also suggested to be negligible in austral summer 2013 during cruise M92 due to nominal surface wind stress (Thomsen et al., 2016). Results from studies conducted in the same year (October to December 2013, Kadko, 2017; December 2012, Steinfeldt et al., 2015; January 2013, Thomsen et al., 2016) indicate that seasonal upwelling rates vary drastically in the Peruvian upwelling zone. The seasonal dynamics of coastal upwelling off Peru are similar to those seen in the Arabian Sea, where large upwelled ^{234}Th fluxes only occurred during mid-late southwest monsoon at stations

close to shore (Buesseler et al., 1998). Our findings lend further support to earlier studies that advection and diffusion are seasonally important for ^{234}Th fluxes in regions with high upwelling velocities and diffusivities such as the equatorial Pacific (Bacon et al., 1996; Buesseler et al., 1995; Dunne and Murray, 1999) and coastal sites such as the Arabian Sea (Buesseler et al., 1998) and offshore Peru (Black et al., 2018; this study).

4.3 Residence time of ^{234}Th in the Peruvian OMZ

The residence time calculated using equation (6) was based on a simplified one-dimension (1D) model of Zimmerman (1976). This 1D steady state model is obviously an oversimplification of a multi-dimensional process, it however provides a good first order estimate for understanding the highly dynamic nature of the ^{234}Th residence time. It also provides a reasonable value that can be directly compared to values estimated in earlier ^{234}Th flux studies that did not consider the physical processes. Furthermore, we showed in the Discussion (sections 4.2) that physical processes, namely upwelling and vertical diffusion, are only important at a few shelf stations. We thus consider this simple 1D model robust in estimating the residence time of total ^{234}Th.

In this study, residence time of total ^{234}Th in the top layer varied from 20 days at shallow stations to 95 days at deep stations (mean $\tau = 51 \pm 23$ days, 1SD, n = 24; Table 3). These values were similar to those estimated within the California Current (Coale and Bruland, 1985) and the residence times of particulate organic carbon (POC) and nitrogen (PON) (Murray et al., 1989), but were much longer than predicted in nearshore shelf waters where residence times of total ^{234}Th were on the order of a few days (Kaufman et al., 1981; Kim et al., 1999; and references therein). The longer residence times estimated in our study could reflect a combination of weak surface ^{234}Th deficits (^{234}Th = 0.63 to 1.82 dpm L^{-1}) (Figure 3) and low export fluxes (800 to 2000 dpm m^{-2} d^{-1}, Figure 7). Nearshore seawater

553 samples during GP16 (Black et al., 2018) featured similar surface ^{234}Th deficits (^{234}Th = 0.63
554 to 1.33 dpm L^{-1}) but much higher downward ^{234}Th fluxes (4000 to 5000 dpm m^{-2} d^{-1}) as a
555 result of strong upwelling, implying that residence times of total ^{234}Th in the Peruvian OMZ
556 during GP16 occupation would be 3 – 6 times shorter. Indeed, a quick re-assessment of the
557 GP16 data predicted a shorter residence time of total ^{234}Th of 5 – 23 days within the euphotic
558 zone of the coastal Peruvian OMZ.

559 These temporal variations on the residence times of total ^{234}Th have important
560 implications for the estimation of POC fluxes and quantification of carbon export efficiency.
561 Firstly, seasonal changes in Th residence times reflect variations in particle removal over
562 different integrated timescales. For example, POC produced in surface waters during GP16
563 (austral spring 2013) (Black et al., 2018) would have been exported out of the euphotic zone
564 3-6 times faster than it did during austral autumn 2017 (this study). Secondly, to properly
565 evaluate carbon export efficiency, surface net primary production (NPP) should be averaged
566 over a similar timescale as the residence time of total ^{234}Th during station occupation.
567 Applying a 16-day averaged NPP for export efficiency estimate (Black et al., 2018; Henson et
568 al., 2011) would likely not be appropriate in the current study in which total ^{234}Th fluxes
569 integrated timescales of several weeks. ^{234}Th residence times should thus be properly
570 quantified in coastal studies before deriving export efficiencies over varying NPP integration
571 timescales.

572

573 **5. Conclusions and implications for coastal ^{234}Th flux studies**

574 Advection and diffusion are important in coastal and upwelling regions with respect to
575 ^{234}Th export fluxes (Bacon et al., 1996; Buesseler et al., 1995; Dunne and Murray, 1999;
576 Buesseler et al., 1998). Our findings show that their significance is subject to the seasonal
577 variability of the current and upwelling velocities, diffusivities and ^{234}Th gradients, and

should be evaluated on a case-to-case basis. Advective fluxes are perhaps the most straightforward to estimate as current velocities can be obtained routinely from shipboard ADCP measurements and upwelling rates calculated from satellite wind stress (Steinfeldt et al., 2015; Bacon et al., 1996). Horizontal and vertical velocities derived from general ocean circulation models also provide a good first order estimate for advective ^{234}Th fluxes; this approach has been successfully demonstrated in a few studies (Buesseler et al., 1995; Buesseler et al., 1998). In addition, the anthropogenic SF_6 tracer and radium isotopes, widely used to quantify nutrient and Fe fluxes (Charette et al., 2007; Law et al., 2001), as well as ^{7}Be isotope (Kadko, 2017), could be used independently to constrain horizontal and vertical exchange rates of ^{234}Th (Morris et al., 2007; Charette et al., 2007; Buesseler et al., 2005). When *in situ* microstructure measurements are available (this study), vertical diffusivity can be directly calculated to estimate the vertical diffusive ^{234}Th fluxes. Yet, microstructure analysis is not a routine measurement on oceanographic cruises. Earlier studies in the equatorial Pacific and the Gulf of Maine have shown that general ocean circulation models and a simple assumption on dissipation coefficients could provide a robust estimate on vertical and horizontal diffusivities (Benitez-Nelson et al., 2000; Gustafsson et al., 1998; Charette et al., 2001). Therefore, the calculation of physical fluxes is possible, though challenging, and ^{234}Th fluxes due to physical processes should be carefully considered when conducting research in a coastal and upwelling systems.

A striking finding in this study is that the assumption of a linear ^{238}U-salinity correlation could lead to one of the largest errors in ^{234}Th flux estimates. In our study, using the salinity-based ^{238}U activities resulted in significant underestimation of total ^{234}Th fluxes by as much as 40%. Because the translation of ^{238}U activities to ^{234}Th fluxes is not linear, larger differences between measured and salinity-based ^{238}U do not necessarily contribute to greater overestimation or underestimation of ^{234}Th fluxes. For example, moderate difference of 3-6%

603 in ^{238}U throughout the upper 100 m at station 898 lead to 40% difference in final ^{234}Th flux,
604 while a 5-9% difference in ^{238}U at station 906 only resulted in 16% ^{234}Th flux difference
605 (Table 2, S2). We would thus stress the importance of ^{238}U measurements in future ^{234}Th flux
606 studies particularly in coastal and shelf regions.

607 Finally, our study showed that the residence times of total ^{234}Th in the Peruvian
608 nearshore waters varied seasonally. Tropical OMZs are important hotspots for carbon
609 sequestration from the atmosphere and enhanced sedimentary carbon preservation (Arthur et
610 al., 1998; Suess et al., 1987). These OMZs are projected to intensify as a result of future
611 climate change (Keeling and Garcia, 2002; Schmidtko et al., 2017; Stramma et al., 2008).
612 Future studies should take into consideration the large temporal variations of the residence
613 times of total ^{234}Th in order to properly evaluates how carbon biogeochemical cycles and
614 carbon export efficiency in these OMZs will respond to continuing ocean deoxygenation,

615

616 **Data availability**

617 Data are available in supplementary tables and archived at
618 https://doi.org/10.1594/PANGAEA.921917 (Xie et al., 2020).

619

620 **Author contribution**

621 RCX, FACLM and EAP designed the study. RCX carried out sampling, on-board beta
622 counting of ^{234}Th, and drafted the manuscript. IR conducted ^{234}Th and ^{238}U analyses at home
623 laboratory. JL computed current velocities and vertical diffusivities respectively from
624 VmADCP and microstructure profiler data. All co-authors had a chance to review the
625 manuscript and contributed to discussion and interpretation of the data presented.

Competing interests

The authors declare that they have no conflict of interest.

Acknowledgements

We thank the crew and science party on board M136 and M138 for their help in sample collection and instrument operation. Thank you to SiaoJean Ko, Dominik Jasinski, André Mutzberg and Mario Esposito for their laboratory assistance. We thank two anonymous reviewers and the associate editor, Marilaure Grégoire, for their constructive comments. The project, cruises, IR, JL and RCX were funded by the German SFB 754 program ('Climate-Biogeochemistry Interactions in the Tropical Ocean'), RCX additionally by a DFG research grant (project number 432469432), and FACLM by a DFG Fellowship of the Excellence Cluster "The Future Ocean" (CP1403). This manuscript benefited from stimulating discussions at the BIARRITZ ('bridging international activity and related research into the twilight zone') workshop held in Southampton, UK in 2019.

References

Abernathey, R. P., and Marshall, J.: Global surface eddy diffusivities derived from satellite altimetry, Journal of Geophysical Research: Oceans, 118, 901-916, https://doi.org/10.1002/jgrc.20066, 2013.

Anderson, R. F., Fleisher, M. Q., and LeHuray, A. P.: Concentration, oxidation state, and particulate flux of uranium in the Black Sea, Geochimica et Cosmochimica Acta, 53, 2215-2224, https://doi.org/10.1016/0016-7037(89)90345-1, 1989.

Arthur, M. A., Dean, W. E., and Laarkamp, K.: Organic carbon accumulation and preservation in surface sediments on the Peru margin, Chemical Geology, 152, 273-286, https://doi.org/10.1016/S0009-2541(98)00120-X, 1998.

Bacon, M., Cochran, J., Hirschberg, D., Hammar, T., and Fleer, A.: Export flux of carbon at the equator during the EqPac time-series cruises estimated from ^{234}Th measurements, Deep Sea Research Part II: Topical Studies in Oceanography, 43, 1133-1153, https://doi.org/10.1016/0967-0645(96)00016-1, 1996.

Barnes, C., and Cochran, J.: Uranium removal in oceanic sediments and the oceanic U balance, Earth and Planetary Science Letters, 97, 94-101, https://doi.org/10.1016/0012-821X(90)90101-3, 1990.

Barnes, C. E., and Cochran, J. K.: Geochemistry of uranium in Black Sea sediments, Deep Sea Research Part A. Oceanographic Research Papers, 38, S1237-S1254, https://doi.org/10.1016/S0198-0149(10)80032-9, 1991.

Barnes, C. E., and Cochran, J. K.: Uranium geochemistry in estuarine sediments: Controls on removal and release processes, Geochimica et Cosmochimica Acta, 57, 555-569, https://doi.org/10.1016/0016-7037(93)90367-6, 1993.

Benitez-Nelson, C. R., Buesseler, K. O., and Crossin, G.: Upper ocean carbon export, horizontal transport, and vertical eddy diffusivity in the southwestern Gulf of Maine,

667 Continental Shelf Research, 20, 707-736, https://doi.org/10.1016/S0278-4343(99)00093-X,
668 2000.
669 Bentamy, A., and Croize-Fillon: Gridded surface wind fields from Metop/ASCAT
670 measurements, International Journal of Remote Sensing,
671 DOI:10.1080/01431161.2011.600348, 2010.
672 Bewers, J., and Yeats, P.: Oceanic residence times of trace metals, Nature, 268, 595-598,
673 https://doi.org/10.1038/268595a0, 1977.
674 Bhat, S., Krishnaswamy, S., Lal, D., and Moore, W.: $^{234}Th/^{238}U$ ratios in the ocean, Earth and
675 Planetary Science Letters, 5, 483-491, https://doi.org/10.1016/S0012-821X(68)80083-4, 1968.
676 Black, E. E., Buesseler, K. O., Pike, S. M., and Lam, P. J.: ^{234}Th as a tracer of particulate
677 export and remineralization in the southeastern tropical Pacific, Marine Chemistry, 201, 35-
678 50, https://doi.org/10.1016/j.marchem.2017.06.009, 2018.
679 Black, E. E., Lam, P. J., Lee, J. M., and Buesseler, K. O.: Insights From the ^{238}U - ^{234}Th
680 Method Into the Coupling of Biological Export and the Cycling of Cadmium, Cobalt, and
681 Manganese in the Southeast Pacific Ocean, Global Biogeochemical Cycles, 33, 15-36,
682 https://doi.org/10.1029/2018GB005985, 2019.
683 Böning, P., Brumsack, H.-J., Böttcher, M. E., Schnetger, B., Kriete, C., Kallmeyer, J., and
684 Borchers, S. L.: Geochemistry of Peruvian near-surface sediments, Geochimica et
685 Cosmochimica Acta, 68, 4429-4451, https://doi.org/10.1016/j.gca.2004.04.027, 2004.
686 Buckingham, C. E., Lucas, N. S., Belcher, S. E., Rippeth, T. P., Grant, A. L. M., Le Sommer,
687 J., Ajayi, A. O., and Naveira Garabato, A. C.: The Contribution of Surface and Submesoscale
688 Processes to Turbulence in the Open Ocean Surface Boundary Layer, Journal of Advances in
689 Modeling Earth Systems, 11, 4066-4094, https://doi.org/10.1029/2019MS001801, 2019.
690 Buesseler, K., Ball, L., Andrews, J., Benitez-Nelson, C., Belastock, R., Chai, F., and Chao,
691 Y.: Upper ocean export of particulate organic carbon in the Arabian Sea derived from

692 thorium-234, Deep Sea Research Part II: Topical Studies in Oceanography, 45, 2461-2487,
693 https://doi.org/10.1016/S0967-0645(98)80022-2, 1998.
694 Buesseler, K. O., Bacon, M. P., Cochran, J. K., and Livingston, H. D.: Carbon and nitrogen
695 export during the JGOFS North Atlantic Bloom Experiment estimated from ^{234}Th: ^{238}U
696 disequilibria, Deep Sea Research Part A. Oceanographic Research Papers, 39, 1115-1137,
697 https://doi.org/10.1016/0198-0149(92)90060-7, 1992.
698 Buesseler, K. O., Andrews, J. A., Hartman, M. C., Belastock, R., and Chai, F.: Regional
699 estimates of the export flux of particulate organic carbon derived from thorium-234 during the
700 JGOFS EqPac program, Deep Sea Research Part II: Topical Studies in Oceanography, 42,
701 777-804, https://doi.org/10.1016/0967-0645(95)00043-P, 1995.
702 Buesseler, K. O., Andrews, J., Pike, S. M., Charette, M. A., Goldson, L. E., Brzezinski, M. A.,
703 and Lance, V.: Particle export during the southern ocean iron experiment (SOFeX),
704 Limnology and Oceanography, 50, 311-327, https://doi.org/10.4319/lo.2005.50.1.0311, 2005.
705 Buesseler, K. O., Benitez-Nelson, C. R., Moran, S., Burd, A., Charette, M., Cochran, J. K.,
706 Coppola, L., Fisher, N., Fowler, S., and Gardner, W.: An assessment of particulate organic
707 carbon to thorium-234 ratios in the ocean and their impact on the application of ^{234}Th as a
708 POC flux proxy, Marine Chemistry, 100, 213-233,
709 https://doi.org/10.1016/j.marchem.2005.10.013, 2006.
710 Buesseler, K. O., and Boyd, P. W.: Shedding light on processes that control particle export
711 and flux attenuation in the twilight zone of the open ocean, Limnology and Oceanography, 54,
712 1210-1232, https://doi.org/10.4319/lo.2009.54.4.1210, 2009.
713 Cai, P., Chen, W., Dai, M., Wan, Z., Wang, D., Li, Q., Tang, T., and Lv, D.: A high ‐
714 resolution study of particle export in the southern South China Sea based on ^{234}Th: ^{238}U
715 disequilibrium, Journal of Geophysical Research: Oceans, 113,
716 https://doi.org/10.1029/2007JC004268, 2008.

717 Charette, M. A., Moran, S. B., Pike, S. M., and Smith, J. N.: Investigating the carbon cycle in
718 the Gulf of Maine using the natural tracer thorium 234, Journal of Geophysical Research:
719 Oceans, 106, 11553-11579, https://doi.org/10.1029/1999JC000277, 2001.
720 Charette, M. A., Gonneea, M. E., Morris, P. J., Statham, P., Fones, G., Planquette, H., Salter,
721 I., and Garabato, A. N.: Radium isotopes as tracers of iron sources fueling a Southern Ocean
722 phytoplankton bloom, Deep Sea Research Part II: Topical Studies in Oceanography, 54, 1989-
723 1998, https://doi.org/10.1016/j.dsr2.2007.06.003, 2007.
724 Chen, J., Edwards, R. L., and Wasserburg, G. J.: ^{238}U, ^{234}U and ^{232}Th in seawater, Earth and
725 Planetary Science Letters, 80, 241-251, https://doi.org/10.1016/0012-821X(86)90108-1, 1986.
726 Coale, K. H., and Bruland, K. W.: ^{234}Th: ^{238}U disequilibria within the California Current 1,
727 Limnology and Oceanography, 30, 22-33, https://doi.org/10.4319/lo.1985.30.1.0022, 1985.
728 Coale, K. H., and Bruland, K. W.: Oceanic stratified euphotic zone as elucidated by ^{234}Th:
729 ^{238}U disequilibria 1, Limnology and Oceanography, 32, 189-200,
730 https://doi.org/10.4319/lo.1987.32.1.0189, 1987.
731 Cochran, J., and Masqué, P.: Short-lived U/Th series radionuclides in the ocean: tracers for
732 scavenging rates, export fluxes and particle dynamics, Reviews in Mineralogy and
733 geochemistry, 52, 461-492, https://doi.org/10.2113/0520461, 2003.
734 Dengler, M., and Sommer, S.: Coupled benthic and pelagic oxygen, nutrient and trace metal
735 cycling, ventilation and carbon degradation in the oxygen minimum zone of the Peruvian
736 continental margin (SFB 754): Cruise No. M 136 11.04.–03.05. 2017 Callao (Peru)–Callao
737 Solute-Flux Peru I, METEOR-Berichte, DOI: 10.3289/CR_M136, 2017, 2017.
738 Dunne, J. P., and Murray, J. W.: Sensitivity of ^{234}Th export to physical processes in the
739 central equatorial Pacific, Deep Sea Research Part I: Oceanographic Research Papers, 46,
740 831-854, https://doi.org/10.1016/S0967-0637(98)00098-3, 1999.

741 Echevin, V. M., Colas, F., Espinoza-Morriberon, D., Anculle, T., Vasquez, L., and Gutierrez,
742 D.: Forcings and evolution of the 2017 coastal El Niño off Northern Peru and Ecuador,
743 Frontiers in Marine Science, 5, 367, https://doi.org/10.3389/fmars.2018.00367, 2018.
744 Fischer, J., Brandt, P., Dengler, M., Müller, M., and Symonds, D.: Surveying the upper ocean
745 with the Ocean Surveyor: a new phased array Doppler current profiler, Journal of
746 Atmospheric and Oceanic Technology, 20, 742-751, https://doi.org/10.1175/1520-
747 0426(2003)20<742:STUOWT>2.0.CO;2, 2003.
748 Garreaud, R. D.: A plausible atmospheric trigger for the 2017 coastal El Niño, International
749 Journal of Climatology, 38, e1296-e1302, https://doi.org/10.1002/joc.5426, 2018.
750 Gregg, M., D'Asaro, E., Riley, J., and Kunze, E.: Mixing efficiency in the ocean, Annual
751 review of marine science, 10, 443-473, DOI: 10.1146/annurev-marine-121916-063643, 2018.
752 Gustafsson, Ö., Buesseler, K. O., Rockwell Geyer, W., Bradley Moran, S., and Gschwend, P.
753 M.: An assessment of the relative importance of horizontal and vertical transport of particle-
754 reactive chemicals in the coastal ocean, Continental Shelf Research, 18, 805-829,
755 https://doi.org/10.1016/S0278-4343(98)00015-6, 1998.
756 Hahn, J., Brandt, P., Greatbatch, R. J., Krahmann, G., and Körtzinger, A.: Oxygen variance
757 and meridional oxygen supply in the Tropical North East Atlantic oxygen minimum zone,
758 Climate dynamics, 43, 2999-3024, https://doi.org/10.1007/s00382-014-2065-0, 2014.
759 Henson, S. A., Sanders, R., Madsen, E., Morris, P. J., Le Moigne, F., and Quartly, G. D.: A
760 reduced estimate of the strength of the ocean's biological carbon pump, Geophysical Research
761 Letters, 38, DOI: 10.1029/2011gl046735, 2011.
762 Kadko, D.: Upwelling and primary production during the US GEOTRACES East Pacific
763 Zonal Transect, Global Biogeochemical Cycles, 31, 218-232,
764 https://doi.org/10.1002/2016GB005554, 2017.

765 Kaufman, A., Li, Y.-H., and Turekian, K. K.: The removal rates of ^{234}Th and ^{228}Th from
766 waters of the New York Bight, Earth and Planetary Science Letters, 54, 385-392,
767 https://doi.org/10.1016/0012-821X(81)90054-6, 1981.
768 Keeling, R. F., and Garcia, H. E.: The change in oceanic O_2 inventory associated with recent
769 global warming, Proceedings of the National Academy of Sciences, 99, 7848-7853, DOI:
770 10.1073/pnas.122154899, 2002.
771 Kim, G., Hussain, N., and Church, T. M.: How accurate are the ^{234}Th based particulate
772 residence times in the ocean?, Geophysical research letters, 26, 619-622,
773 https://doi.org/10.1029/1999GL900037, 1999.
774 Ku, T.-L., Knauss, K. G., and Mathieu, G. G.: Uranium in open ocean: concentration and
775 isotopic composition, Deep Sea Research, 24, 1005-1017, https://doi.org/10.1016/0146-
776 6291(77)90571-9, 1977.
777 Law, C., Martin, A., Liddicoat, M., Watson, A., Richards, K., and Woodward, E.: A
778 Lagrangian SF6 tracer study of an anticyclonic eddy in the North Atlantic: Patch evolution,
779 vertical mixing and nutrient supply to the mixed layer, Deep Sea Research Part II: Topical
780 Studies in Oceanography, 48, 705-724, https://doi.org/10.1016/S0967-0645(00)00112-0,
781 2001.
782 Le Moigne, F. A. C., Henson, S. A., Sanders, R. J., and Madsen, E.: Global database of
783 surface ocean particulate organic carbon export fluxes diagnosed from the ^{234}Th technique,
784 Earth Syst. Sci. Data, 5, 295-304, https://doi.org/10.5194/essd-5-295-2013, 2013.
785 Lee, C., Murray, D., Barber, R., Buesseler, K., Dymond, J., Hedges, J., Honjo, S., Manganini,
786 S., Marra, J., and Moser, C.: Particulate organic carbon fluxes: compilation of results from the
787 1995 US JGOFS Arabian Sea process study: By the Arabian Sea carbon flux group, Deep Sea
788 Research Part II: Topical Studies in Oceanography, 45, 2489-2501,
789 https://doi.org/10.1016/S0967-0645(98)00079-4, 1998.

790 Lüdke, J., Dengler, M., Sommer, S., Clemens, D., Thomsen, S., Krahmann, G., Dale, A. W.,
791 Achterberg, E. P., and Visbeck, M.: Influence of intraseasonal eastern boundary circulation
792 variability on hydrography and biogeochemistry off Peru, Ocean Sci. Discuss., 2019, 1-31,
793 https://doi.org/10.5194/os-2019-93, in review 2020.
794 McDougall, T., Feistel, R., Millero, F., Jackett, D., Wright, D., King, B., Marion, G., Chen,
795 C., Spitzer, P., and Seitz, S.: The International Thermodynamic Equation Of Seawater 2010
796 (TEOS-10): Calculation and Use of Thermodynamic Properties, Global Ship-based Repeat
797 Hydrography Manual, IOCCP Report No, 14, 2009.
798 McKee, B. A., DeMaster, D. J., and Nittrouer, C. A.: Uranium geochemistry on the Amazon
799 shelf: Evidence for uranium release from bottom sediments, Geochimica et Cosmochimica
800 Acta, 51, 2779-2786, https://doi.org/10.1016/0016-7037(87)90157-8, 1987.
801 Morris, P. J., Sanders, R., Turnewitsch, R., and Thomalla, S.: ^{234}Th-derived particulate
802 organic carbon export from an island-induced phytoplankton bloom in the Southern Ocean,
803 Deep Sea Research Part II: Topical Studies in Oceanography, 54, 2208-2232,
804 https://doi.org/10.1016/j.dsr2.2007.06.002, 2007.
805 Murray, J. W., Downs, J. N., Strom, S., Wei, C.-L., and Jannasch, H. W.: Nutrient
806 assimilation, export production and ^{234}Th scavenging in the eastern equatorial Pacific, Deep
807 Sea Research Part A. Oceanographic Research Papers, 36, 1471-1489,
808 https://doi.org/10.1016/0198-0149(89)90052-6, 1989.
809 Nameroff, T., Balistrieri, L., and Murray, J.: Suboxic trace metal geochemistry in the eastern
810 tropical North Pacific, Geochimica et Cosmochimica Acta, 66, 1139-1158,
811 https://doi.org/10.1016/S0016-7037(01)00843-2, 2002.
812 Noffke, A., Hensen, C., Sommer, S., Scholz, F., Bohlen, L., Mosch, T., Graco, M., and
813 Wallmann, K.: Benthic iron and phosphorus fluxes across the Peruvian oxygen minimum
814 zone, Limnology and Oceanography, 57, 851-867, https://doi.org/10.4319/lo.2012.57.3.0851,
815 2012.

816 Osborn, T.: Estimates of the local rate of vertical diffusion from dissipation measurements,
817 Journal of physical oceanography, 10, 83-89, https://doi.org/10.1175/1520-
818 0485(1980)010<0083:EOTLRO>2.0.CO;2, 1980.
819 Owens, S., Buesseler, K., and Sims, K.: Re-evaluating the ^{238}U-salinity relationship in
820 seawater: Implications for the ^{238}U–^{234}Th disequilibrium method, Marine Chemistry, 127, 31-
821 39, https://doi.org/10.1016/j.marchem.2011.07.005, 2011.
822 Owens, S. A., Pike, S., and Buesseler, K. O.: Thorium-234 as a tracer of particle dynamics
823 and upper ocean export in the Atlantic Ocean, Deep Sea Research Part II: Topical Studies in
824 Oceanography, 116, 42-59, http://dx.doi.org/10.1016/j.dsr2.2014.11.010, 2015.
825 Peng, Q., Xie, S.-P., Wang, D., Zheng, X.-T., and Zhang, H.: Coupled ocean-atmosphere
826 dynamics of the 2017 extreme coastal El Niño, Nature Communications, 10, 298, DOI:
827 10.1038/s41467-018-08258-8, 2019.
828 Pike, S., Buesseler, K., Andrews, J., and Savoye, N.: Quantification of ^{234}Th recovery in small
829 volume sea water samples by inductively coupled plasma-mass spectrometry, Journal of
830 Radioanalytical and Nuclear Chemistry, 263, 355-360, https://doi.org/10.1007/s10967-005-
831 0594-z, 2005.
832 Puigcorbé, V., Masqué, P., and Le Moigne, F. A. C.: Global database of ratios of particulate
833 organic carbon to thorium-234 in the ocean: improving estimates of the biological carbon
834 pump, Earth Syst. Sci. Data, 12, 1267-1285, DOI: 10.5194/essd-12-1267-2020, 2020.
835 Rapp, I., Schlosser, C., Menzel Barraqueta, J. L., Wenzel, B., Lüdke, J., Scholten, J., Gasser,
836 B., Reichert, P., Gledhill, M., Dengler, M., and Achterberg, E. P.: Controls on redox-sensitive
837 trace metals in the Mauritanian oxygen minimum zone, Biogeosciences, 16, 4157-4182, DOI:
838 10.5194/bg-16-4157-2019, 2019.
839 Rengarajan, R., Sarin, M., and Krishnaswami, S.: Uranium in the Arabian Sea: role of
840 denitrification in controlling its distribution, Oceanologica acta, 26, 687-693,
841 https://doi.org/10.1016/j.oceact.2003.05.001, 2003.

842 Resplandy, L., Martin, A. P., Le Moigne, F., Martin, P., Aquilina, A., Mémery, L., Lévy, M.,
843 and Sanders, R.: How does dynamical spatial variability impact ^{234}Th-derived estimates of
844 organic export?, Deep Sea Research Part I: Oceanographic Research Papers, 68, 24-45,
845 https://doi.org/10.1016/j.dsr.2012.05.015, 2012.
846 Roquet, F., Madec, G., McDougall, T. J., and Barker, P. M.: Accurate polynomial expressions
847 for the density and specific volume of seawater using the TEOS-10 standard, Ocean
848 Modelling, 90, 29-43, https://doi.org/10.1016/j.ocemod.2015.04.002, 2015.
849 Rosengard, S. Z., Lam, P. J., Balch, W. M., Auro, M. E., Pike, S., Drapeau, D., and Bowler,
850 B.: Carbon export and transfer to depth across the Southern Ocean Great Calcite Belt,
851 DOI:10.5194/bg-12-3953-2015, 2015.
852 Santschi, P., Murray, J. W., Baskaran, M., Benitez-Nelson, C. R., Guo, L., Hung, C.-C.,
853 Lamborg, C., Moran, S., Passow, U., and Roy-Barman, M.: Thorium speciation in seawater,
854 Marine Chemistry, 100, 250-268, https://doi.org/10.1016/j.marchem.2005.10.024, 2006.
855 Savoye, N., Benitez-Nelson, C., Burd, A. B., Cochran, J. K., Charette, M., Buesseler, K. O.,
856 Jackson, G. A., Roy-Barman, M., Schmidt, S., and Elskens, M.: ^{234}Th sorption and export
857 models in the water column: a review, Marine Chemistry, 100, 234-249,
858 https://doi.org/10.1016/j.marchem.2005.10.014, 2006.
859 Schafstall, J., Dengler, M., Brandt, P., and Bange, H.: Tidal‐induced mixing and diapycnal
860 nutrient fluxes in the Mauritanian upwelling region, Journal of Geophysical Research:
861 Oceans, 115, https://doi.org/10.1029/2009jc005940, 2010, 2010.
862 Schmidt, S., and Reyss, J.: Uranium concentrations of Mediterranean seawater with high
863 salinities, Comptes Rendus de l'Academie des Sciences. Serie 2, 312, 479-484, 1991.
864 Schmidtko, S., Stramma, L., and Visbeck, M.: Decline in global oceanic oxygen content
865 during the past five decades, Nature, 542, 335, DOI: 10.1038/nature21399, 2017.
866 Scholz, F., Hensen, C., Noffke, A., Rohde, A., Liebetrau, V., and Wallmann, K.: Early
867 diagenesis of redox-sensitive trace metals in the Peru upwelling area–response to ENSO-

related oxygen fluctuations in the water column, Geochimica et Cosmochimica Acta, 75, 7257-7276, DOI: 10.1016/j.gca.2011.08.007, 2011.

Scholz, F., McManus, J., Mix, A. C., Hensen, C., and Schneider, R. R.: The impact of ocean deoxygenation on iron release from continental margin sediments, Nature Geosci, 7, 433-437, https://doi.org/10.1038/ngeo2162, 2014.

Shepherd, J. G., Brewer, P. G., Oschlies, A., and Watson, A. J.: Ocean ventilation and deoxygenation in a warming world: introduction and overview, Philosophical Transactions of the Royal Society A: Mathematical, Physical and Engineering Sciences, 375, 20170240, DOI:10.1098/rsta.2017.0240, 2017.

Smith, S. D.: Coefficients for sea surface wind stress, heat flux, and wind profiles as a function of wind speed and temperature, Journal of Geophysical Research: Oceans, 93, 15467-15472, https://doi.org/10.1029/JC093iC12p15467, 1988.

Steinfeldt, R., Sültenfuß, J., Dengler, M., Fischer, T., and Rhein, M.: Coastal upwelling off Peru and Mauritania inferred from helium isotope disequilibrium, Biogeosciences, 12, 7519-7533, https://doi.org/10.5194/bg-12-7519-2015, 2015.

Stramma, L., Johnson, G. C., Sprintall, J., and Mohrholz, V.: Expanding oxygen-minimum zones in the tropical oceans, science, 320, 655-658, DOI: 10.1126/science.1153847, 2008.

Suess, E., Kulm, L., and Killingley, J.: Coastal upwelling and a history of organic-rich mudstone deposition off Peru, Geological Society, London, Special Publications, 26, 181-197, https://doi.org/10.1144/GSL.SP.1987.026.01.11, 1987.

Swarzenski, P., Campbell, P., Porcelli, D., and McKee, B.: The estuarine chemistry and isotope systematics of ^{234,238}U in the Amazon and Fly Rivers, Continental Shelf Research, 24, 2357-2372, https://doi.org/10.1016/j.csr.2004.07.025, 2004.

Thomsen, S., Kanzow, T., Krahmann, G., Greatbatch, R. J., Dengler, M., and Lavik, G.: The formation of a subsurface anticyclonic eddy in the Peru‐Chile Undercurrent and its impact

on the near‐coastal salinity, oxygen, and nutrient distributions, Journal of Geophysical Research: Oceans, 121, 476-501, https://doi.org/10.1002/2015JC010878, 2016.

Van Der Loeff, M. R., Sarin, M. M., Baskaran, M., Benitez-Nelson, C., Buesseler, K. O., Charette, M., Dai, M., Gustafsson, Ö., Masque, P., and Morris, P. J.: A review of present techniques and methodological advances in analyzing ^{234}Th in aquatic systems, Marine Chemistry, 100, 190-212, https://doi.org/10.1016/j.marchem.2005.10.012, 2006.

Waples, J. T., Benitez-Nelson, C., Savoye, N., van der Loeff, M. R., Baskaran, M., and Gustafsson, Ö.: An introduction to the application and future use of ^{234}Th in aquatic systems, Marine Chemistry, 100, 166-189, https://doi.org/10.1016/j.marchem.2005.10.011, 2006.

Weinstein, S. E., and Moran, S. B.: Vertical flux of particulate Al, Fe, Pb, and Ba from the upper ocean estimated from ^{234}Th/^{238}U disequilibria, Deep Sea Research Part I: Oceanographic Research Papers, 52, 1477-1488, https://doi.org/10.1016/j.dsr.2005.03.008, 2005.

Xie, R. C., Le Moigne, F. A. C., Rapp, I., Lüdke, J., Gasser, B., Degnler, M., Liebetrau, V., and Achterberg, E. P.: Activities of total 234Th and dissolved 238U during cruises M136 and M138 from the Peruvian Oxygen Minimum Zone., PANGAEA, https://doi.org/10.1594/PANGAEA.921917, 2020.

Zhurbas, V., and Oh, I. S.: Drifter‐derived maps of lateral diffusivity in the Pacific and Atlantic oceans in relation to surface circulation patterns, Journal of Geophysical Research: Oceans, 109, https://doi.org/10.1029/2003JC002241, 2004.

Zimmerman, J. T. F.: Mixing and flushing of tidal embayments in the western Dutch Wadden Sea part I: Distribution of salinity and calculation of mixing time scales, Netherlands Journal of Sea Research, 10, 149-191, https://doi.org/10.1016/0077-7579(76)90013-2, 1976.

Figure captions

Figure 1. Maps showing (a) locations of each station from M136 (white squares) and M138 (grey circles) and (B) monthly-averaged current field in the top 15 m from April 16 to May 15, 2017 derived from altimetry measurements (http://marine.copernicus.eu/; product ID: MULTIOBS_GLO-PHY_REP_015_004). Color boxes in (a) schematically divide the four shelf-offshore transects. Map (a) was created with Ocean Data View (Schlitzer, 2014). The white box in (b) highlights our study area.

Figure 2. Profiles of ^{238}U (black) and ^{234}Th (orange squares – M136; orange circles – M138) along with concentrations of oxygen (grey) and fluorescence (green). Profiles are organized by cruises, transects, and distance to shore from left to right and top to bottom, indicated by east (E) to west (W) arrows. Error bars for both ^{238}U and ^{234}Th are indicated. Red dashed lines indicate the depth of the mixed layer. The start of the oxygen deficient zone is where oxygen diminishes. Bottom depths are indicated for stations whose bottom depths are shallower than 600 m.

Figure 3. Shelf-offshore distributions of $^{234}Th/^{238}U$ along the four studied transects, as shown in Figure 1, for M136 (left) and M138 (right). White dots denote station location.

Figure 4. Distributions of averaged ^{234}Th activities during M136 (a, top 30 m) and M138 (b, top 50 m).

940 Figure 5. Profiles of temperature (solid lines) and salinity (dashed lines) for (a) repeated
941 stations 458 (purple) and 508 (yellow), and (d) 495 (blue) and 516 (orange); (b) and (c)
942 respectively profiles for stations 458 and 508 of ^{238}U (black), ^{234}Th (color squares), and
943 concentrations of oxygen (grey) and fluorescence (green). (e) and (f) respectively profiles for
944 stations 495and 516 of ^{238}U (black), ^{234}Th (color squares), and concentrations of oxygen
945 (grey) and fluorescence (green).

946

947 Figure 6. Bar charts of ^{234}Th fluxes due to production and decay (blue), upwelling (orange),
948 and vertical diffusion (grey) for the depths at 5 – 20 m below the ML (top) and 100 m below
949 sea surface (bottom). Color boxes corresponds to individual transects in Figure 1. Within each
950 transect stations from west (offshore) to east (nearshore) are listed from left to right. Error
951 bars (1SE) are indicated.

952

953 Figure 7. Cross plots of measured ^{238}U activities vs. salinity for M136 (a) and M138 (b),
954 showing poor linear relationship between ^{238}U and salinity. (c) shows a direct comparison
955 between measured and salinity-based ^{238}U to further highlight the large difference between the
956 two. The solid blue line indicates the 1:1 ratio between measured and projected ^{238}U. Blue
957 dashed lines indicate the ± errors reported in Owens et al. (2011). Error bars for measured
958 ^{238}U activities are smaller than symbols.

Table 1. ^{234}Th fluxes due to production and decay, upwelling and vertical diffusion below the mixed layer and at 100 m. Horizontal advective fluxes were not quantified at 100 m. Refer to text for details.

							^{234}Th flux at the base of the ML					^{234}Th flux at 100 m				
Cruise	Station	Cast	Mixed layer depth m	Upper oxycline depth m	Maximum fluorescence µg L^{-1}	Equilibrium depth m	Depth m	Production and decay dpm m^{-2} d^{-1}	Upwelling dpm m^{-2} d^{-1}	Diffusion dpm m^{-2} d^{-1}	Final flux dpm m^{-2} d^{-1}	1 SD dpm m^{-2} d^{-1}	Production and decay dpm m^{-2} d^{-1}	Upwelling dpm m^{-2} d^{-1}	Diffusion dpm m^{-2} d^{-1}	Final flux dpm m^{-2} d^{-1}	1 SD dpm m^{-2} d^{-1}
M136	353	1	25	102	1.20	100	30	907	52	-36	923	69	1422	-14	2	1410	189
M136	380	1	26	129	0.87	80	30	1145	0	-41	1105	54	1637	0	-1	1637	132
M136	402	1	24	129	7.51	100	30	808	0	-75	732	64	1234	0	2	1236	111
M136	428	1	10	76	4.11	30	30	983	-128	493	1348	129	1772	33	-390	1415	256
M136	445	1	17	64	2.07	100	30	820	-10	16	826	66	1621	53	6	1681	165
M136	458	1	5	55	1.61	100	30	1012	-18	161	1155	117	2101	-11	145	2235	238
M136	472	1	11	29	7.41	200	40	1887	15	-29	1872	77	3315	-12	63	3366	233
M136	495	1	18	50	1.13	200	30	1149	1	-19	1130	50	3195	2	-5	3192	89
M136	516	1	16	45	3.77	200	30	614	0	1	615	49	2229	2	-4	2227	109
M136	547	1	22	48	1.28	150	30	791	0	85	877	61	2510	0	-15	2495	118
M136	559	1	20	79	1.70	85	50	623	3	-67	559	117	854	-4	2	852	120
M136	567	1	21	50	2.40	150	30	1593	0	-23	1570	52	3011	0	-11	3000	86
M138	879	3	43	93	2.24	200	60	1249	0	-16	1266	91	1702	0	-5	1697	111
M138	882	10	39	211	2.68	150	50	1321	-7	16	1331	63	2264	19	-12	2272	82
M138	883	12	10	220	1.31	250	30	683	-84	-159	758	108	1782	31	-121	1692	179
M138	888	7	41	127	1.59	150	50	1364	0	-120	1244	62	1813	0	-4	1809	86
M138	892	14	47	128	1.05	100	60	1395	33	-118	1309	72	1743	-3	1	1741	99
M138	898	1	38	101	1.42	60	50	1099	0	-19	1080	104	1091	0	0	1091	125
M138	904	16	12	72	3.63	150	20	812	275	0	1087	76	2643	0	-9	2634	79
M138	906	18	32	81	1.73	200	40	1796	0	4	1799	41	3100	0	-1	3100	77
M138	907	11	31	100	1.29	60	60	1594	-88	13	1518	147	1787	67	-2	1853	140
M138	912	3	37	70	2.75	>600	50	1960	0	-79	1881	43	2975	0	-3	2972	78
M138	915	1	26	99	3.51	200	40	1628	0	22	1650	38	2752	0	0	2752	93
M138	919	1	19	79	4.46	150	30	1316	0	49	1365	32	3249	0	-8	3241	85

Table 2. Comparison of ^{234}Th fluxes at 100 m calculated with measured ^{238}U activities and those with salinity-based ^{238}U.

Cruise	Station	Cast	^{234}Th fluxes at 100 m* measured dpm m^{-2} d^{-1}	predicted dpm m^{-2} d^{-1}	Difference %
M136	353	1	1422	1320	8
M136	380	1	1637	1304	26
M136	402	1	1234	865	43
M136	428	1	1772	1443	23
M136	445	1	1621	1365	19
M136	458	1	2101	1859	13
M136	472	1	3315	3073	8
M136	495	1	3195	3058	4
M136	516	1	2229	2140	4
M136	547	1	2510	2313	9
M136	559	1	854	751	14
M136	567	1	3011	2879	5
M138	879	3	1702	1515	12
M138	882	10	2264	1875	21
M138	883	12	1782	1352	32
M138	888	7	1813	1441	26
M138	892	14	1743	1257	39
M138	898	1	1091	770	42
M138	904	16	2643	2280	16
M138	906	18	3100	2673	16
M138	907	11	1787	1308	37
M138	912	3	2975	2572	16
M138	915	1	2752	2380	16
M138	919	1	3249	2862	14

* For comparison purposes, we only report here ^{234}Th fluxes due to radioactive production and decay.

Table 3. Residence time of total ^{234}Th in the top layers of Peruvian OMZ.

Cruise	Station	Cast	Average ^{234}Th in the top layer* dpm L^{-1}	Residence time days
M136	353	1	1.48	46
M136	380	1	1.35	35
M136	402	1	1.64	61
M136	428	1	1.57	35
M136	445	1	1.64	61
M136	458	1	1.45	38
M136	472	1	0.93	20
M136	495	1	1.20	31
M136	516	1	1.74	85
M136	547	1	1.67	63
M136	559	1	1.75	94
M136	567	1	1.41	45
M138	879	3	1.59	75
M138	882	10	1.81	69
M138	883	12	1.87	74
M138	888	7	1.68	67
M138	892	14	1.69	65
M138	898	1	1.66	92
M138	904	16	1.32	24
M138	906	18	1.15	25
M138	907	11	1.04	41
M138	912	3	1.25	33
M138	915	1	1.16	28
M138	919	1	1.17	26

* Here 'the top layer' refers to the top 30 m during M136 and top 50 m during M138.

Figure 1

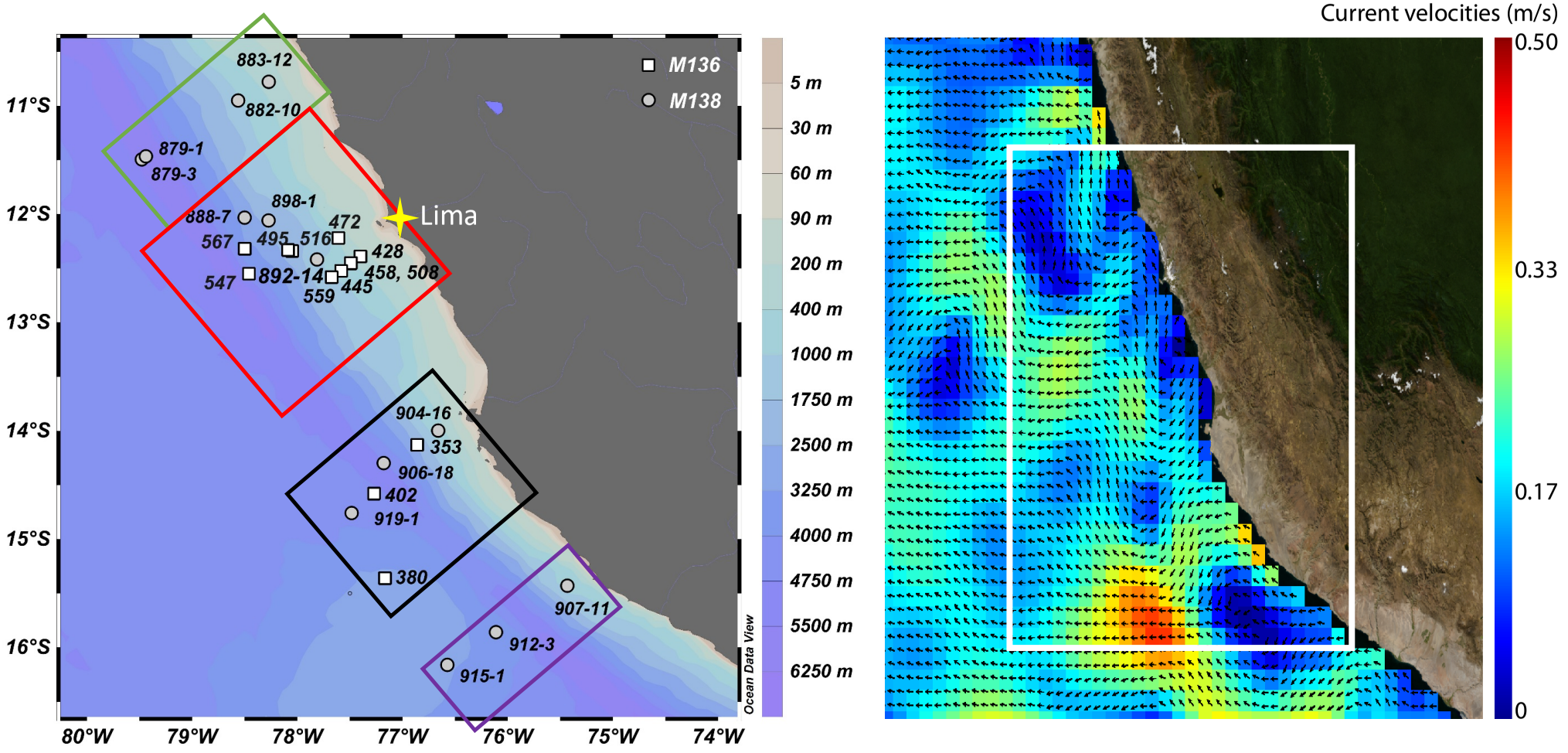
M136
M138
883-12
882-10
879-1
879-3
898-1
888-7
472
Lima
567
495
516
428
547
892-14
458, 508
559
445
904-16
353
906-18
402
919-1
380
907-11
912-3
915-1
11°S
12°S
13°S
14°S
15°S
16°S
80°W
79°W
78°W
77°W
76°W
75°W
74°W
Ocean Data View
5 m
30 m
60 m
90 m
200 m
400 m
1000 m
1750 m
2500 m
3250 m
4000 m
4750 m
5500 m
6250 m
Current velocities (m/s)
0.50
0.33
0.17
0

Figure 2

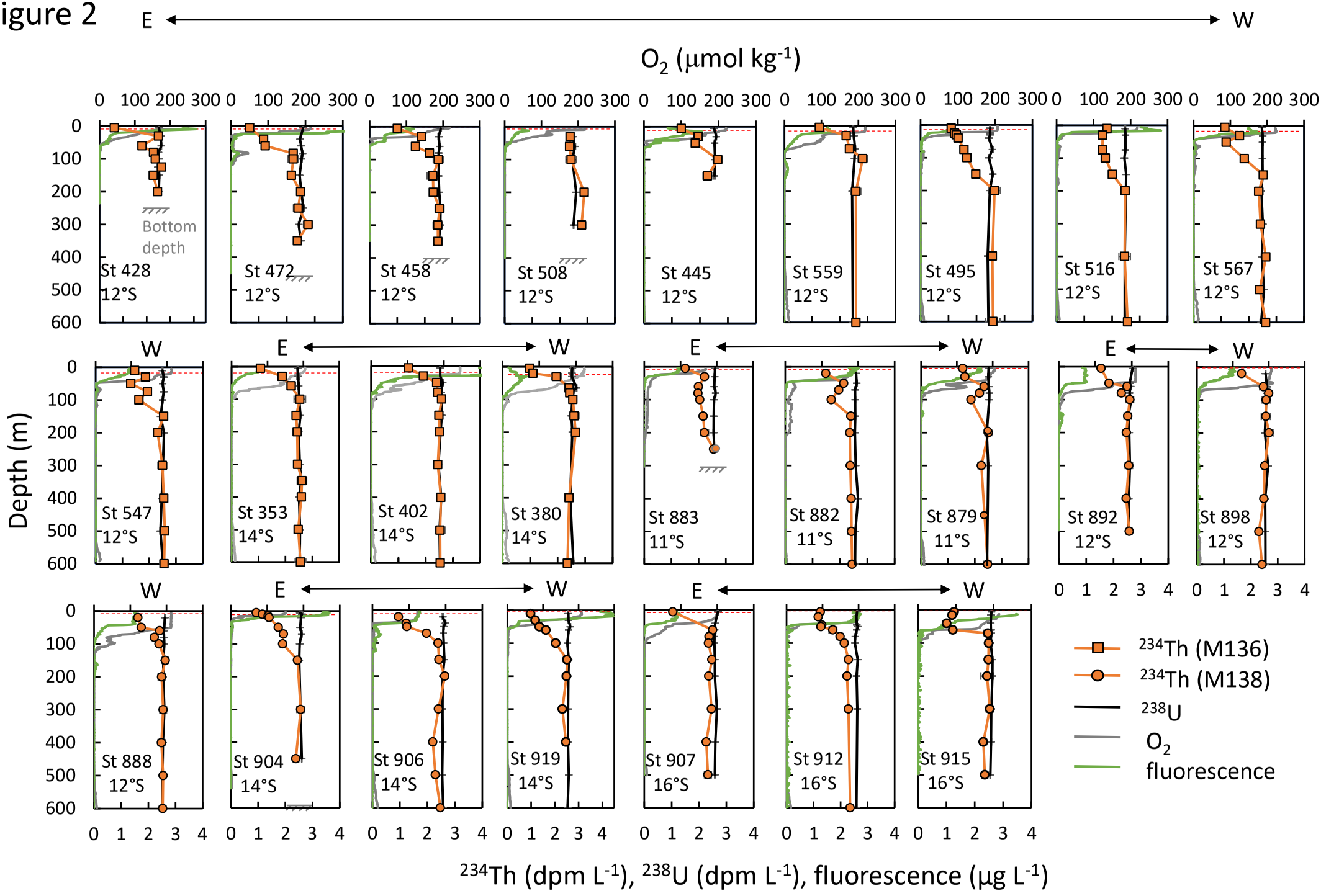
E
W
O2 (µmol kg-1)
0 100 200 300
Depth (m)
Bottom depth
St 428 12°S
St 472 12°S
St 458 12°S
St 508 12°S
St 445 12°S
St 559 12°S
St 495 12°S
St 516 12°S
St 567 12°S
St 547 12°S
St 353 14°S
St 402 14°S
St 380 14°S
St 883 11°S
St 882 11°S
St 879 11°S
St 892 12°S
St 898 12°S
St 888 12°S
St 904 14°S
St 906 14°S
St 919 14°S
St 907 16°S
St 912 16°S
St 915 16°S
0 1 2 3 4
234Th (M136)
234Th (M138)
238U
O2
fluorescence
234Th (dpm L-1), 238U (dpm L-1), fluorescence (µg L-1)

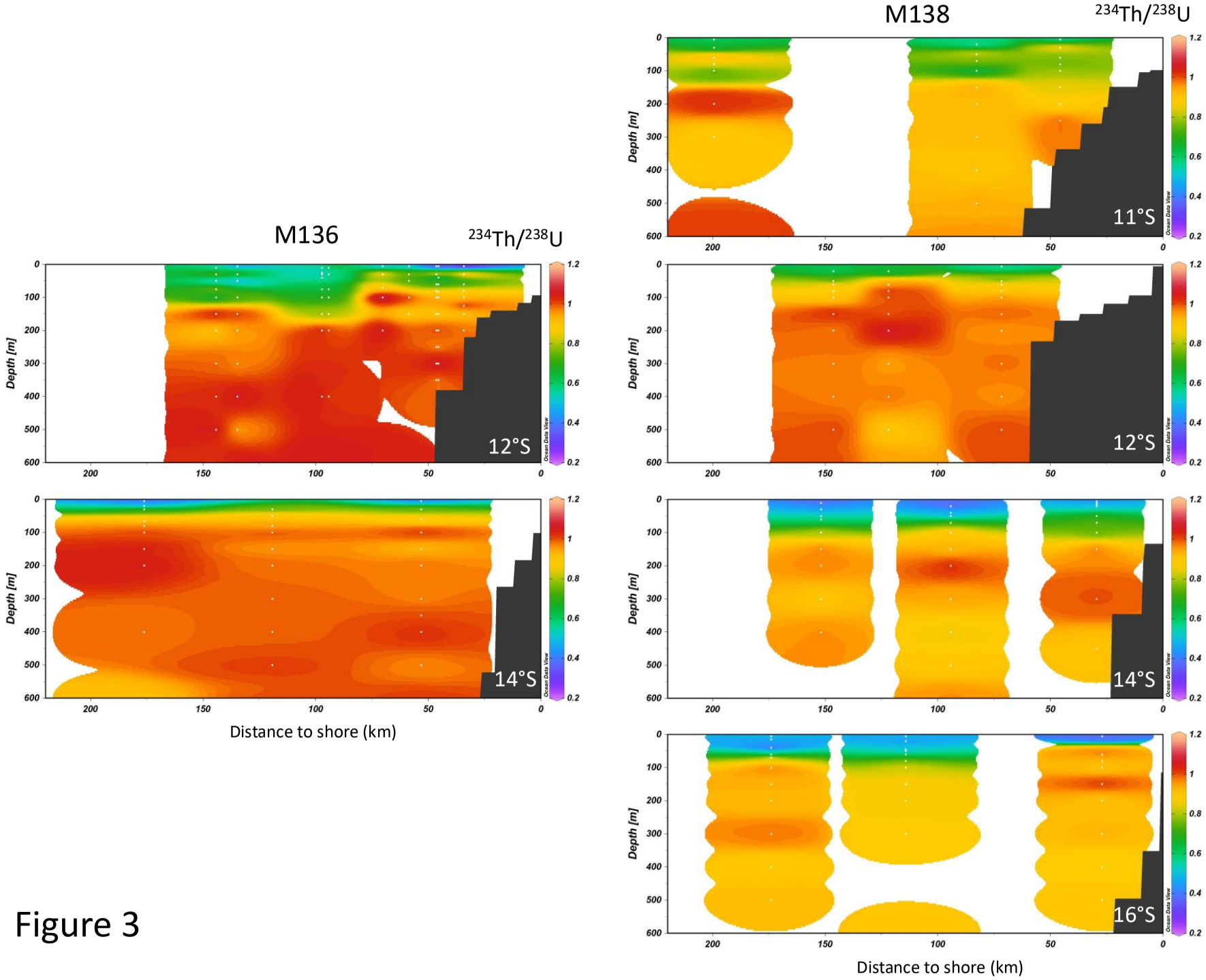
M136
234Th/238U
M138
234Th/238U
12°S
14°S
11°S
12°S
14°S
16°S
Depth [m]
Distance to shore (km)
Distance to shore (km)

Figure 3

Figure 4

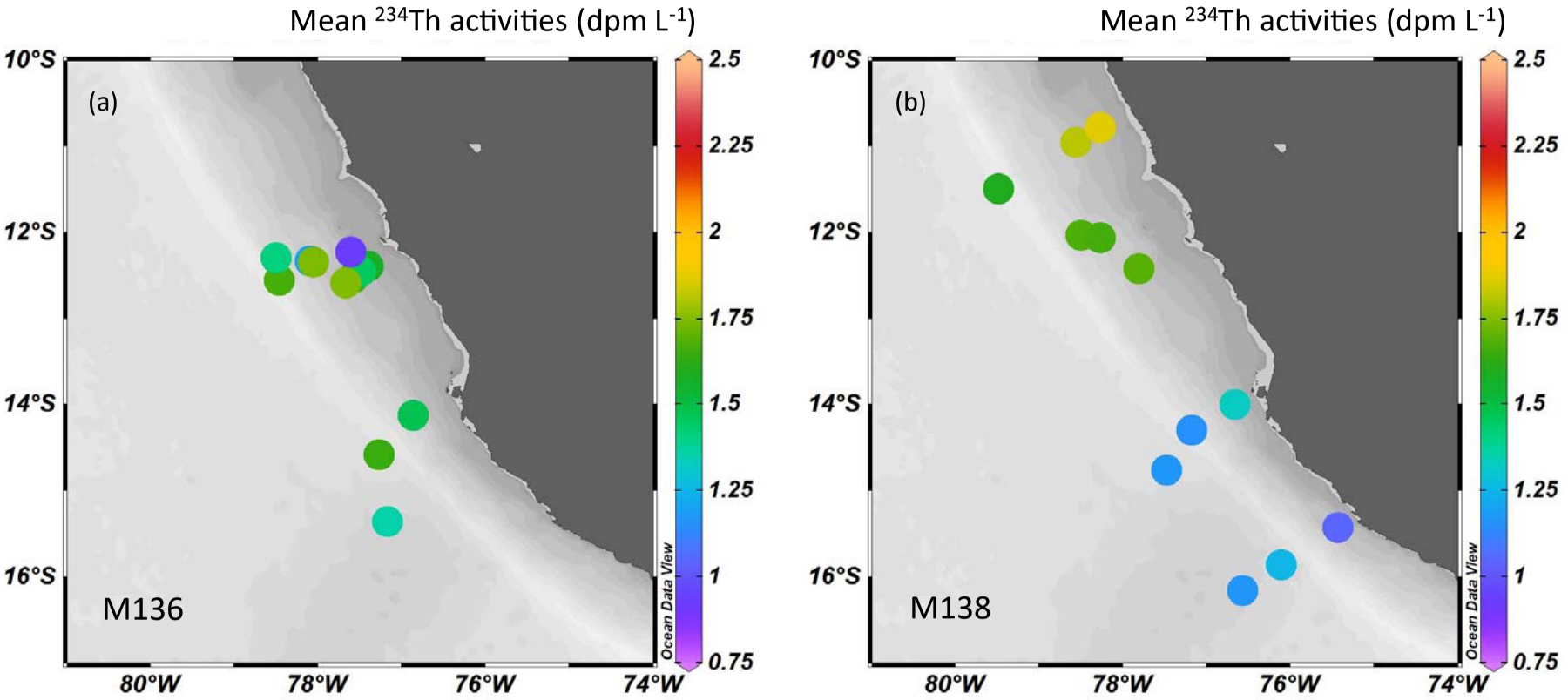
Mean ^{234}Th activities (dpm L^{-1})
(a)
M136
10°S
12°S
14°S
16°S
80°W
78°W
76°W
74°W
2.5
2.25
2
1.75
1.5
1.25
1
0.75
Ocean Data View
Mean ^{234}Th activities (dpm L^{-1})
(b)
M138
10°S
12°S
14°S
16°S
80°W
78°W
76°W
74°W
2.5
2.25
2
1.75
1.5
1.25
1
0.75
Ocean Data View

Figure 5

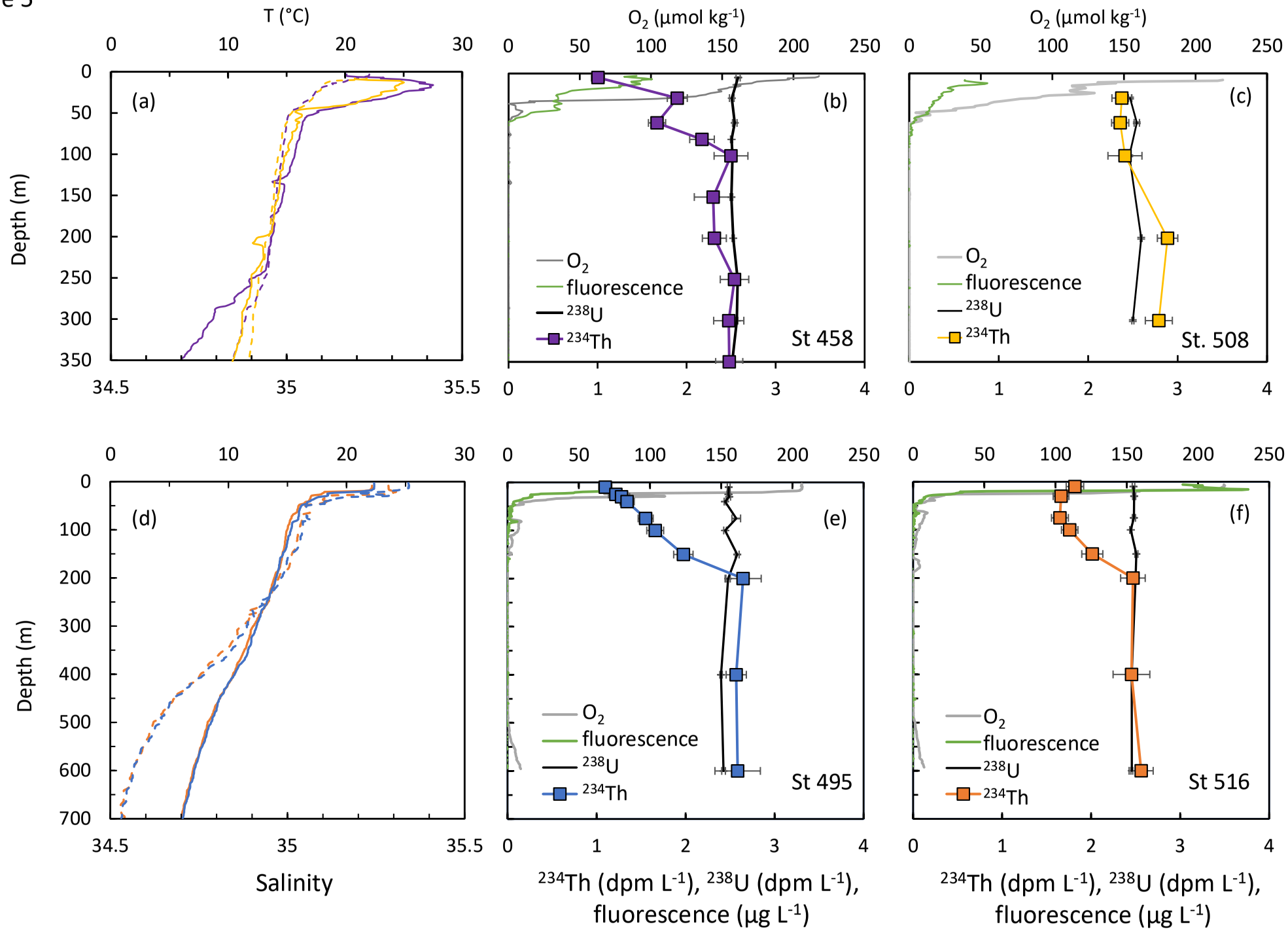
T (°C)
O2 (µmol kg-1)
O2 (µmol kg-1)
Depth (m)
(a)
(b)
(c)
(d)
(e)
(f)
O2
fluorescence
238U
234Th
St 458
St. 508
St 495
St 516
Salinity
234Th (dpm L-1), 238U (dpm L-1), fluorescence (µg L-1)
234Th (dpm L-1), 238U (dpm L-1), fluorescence (µg L-1)

Figure 6

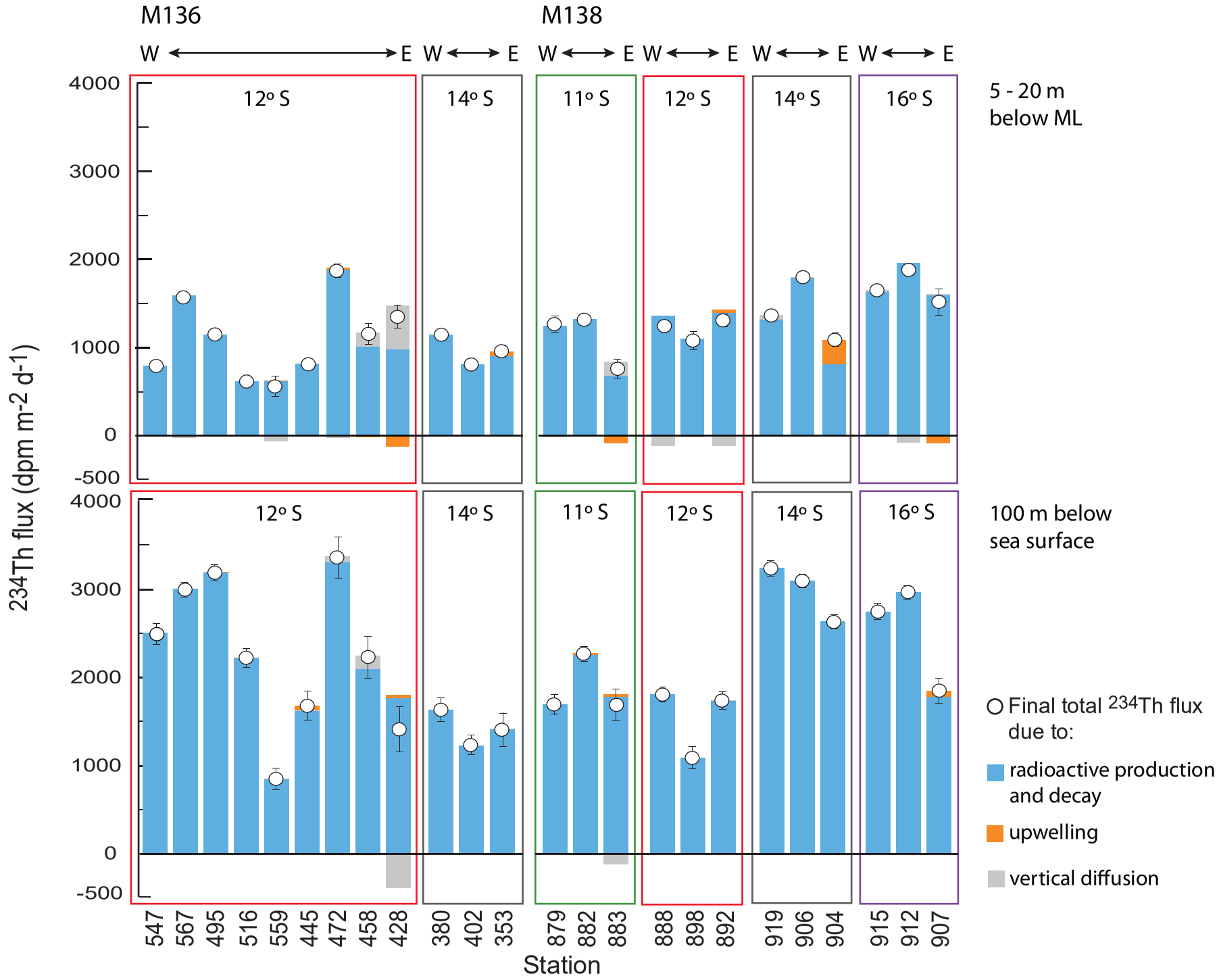
M136
M138
W
E
12° S
14° S
11° S
12° S
14° S
16° S
5 - 20 m below ML
100 m below sea surface
234Th flux (dpm m-2 d-1)
4000
3000
2000
1000
0
-500
547 567 495 516 559 445 472 458 428
380 402 353
879 882 883
888 898 892
919 906 904
915 912 907
Station
Final total 234Th flux due to:
radioactive production and decay
upwelling
vertical diffusion

Figure 7

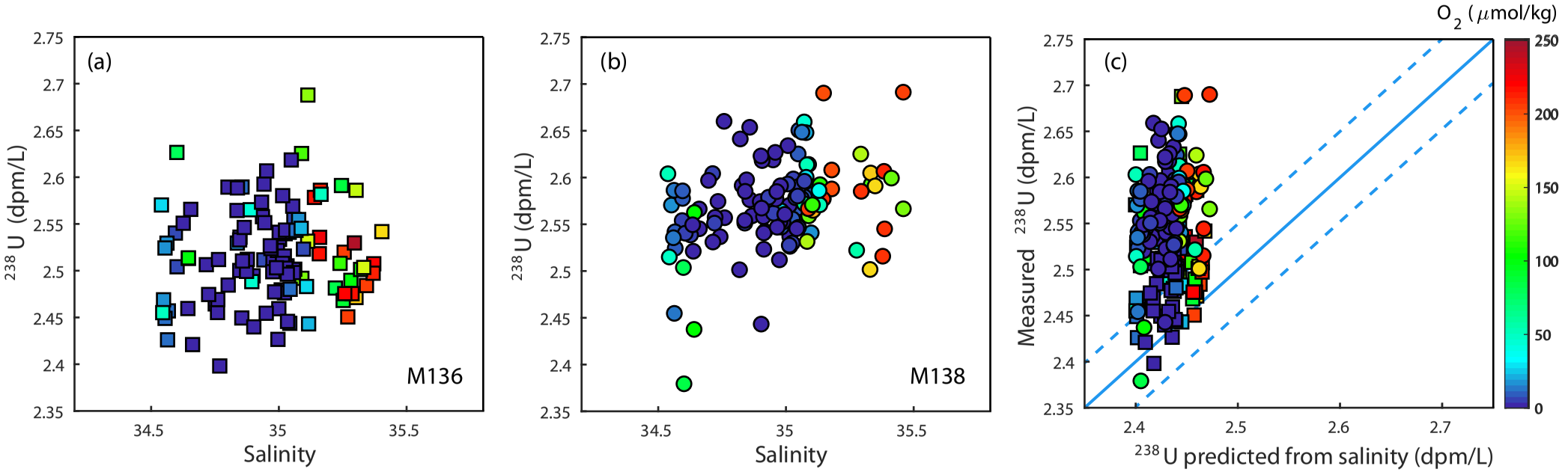
(a)
M136
(b)
M138
(c)
^{238}U (dpm/L)
Salinity
Measured ^{238}U (dpm/L)
^{238}U predicted from salinity (dpm/L)
O_2 (μmol/kg)
2.75
2.7
2.65
2.6
2.55
2.5
2.45
2.4
2.35
34.5
35
35.5
2.4
2.5
2.6
2.7
250
200
150
100
50
0